Supporting Information for

Regional Relative Tectonic Activity of Structures in the Pampean Flat Slab Segment of Argentina from 30 to 32°S

Jeremy M. Rimando [a,b*], Lindsay M. Schoenbohm[a,b]

[a]Department of Earth Sciences, University of Toronto, Toronto, Ontario M5S 3B1, Canada
[b]Department of Chemical and Physical Sciences, University of Toronto Mississauga, Mississauga, Ontario L5L 1C6, Canada
*Corresponding author: jeremy.rimando@mail.utoronto.ca (J. Rimando)

Contents of this file

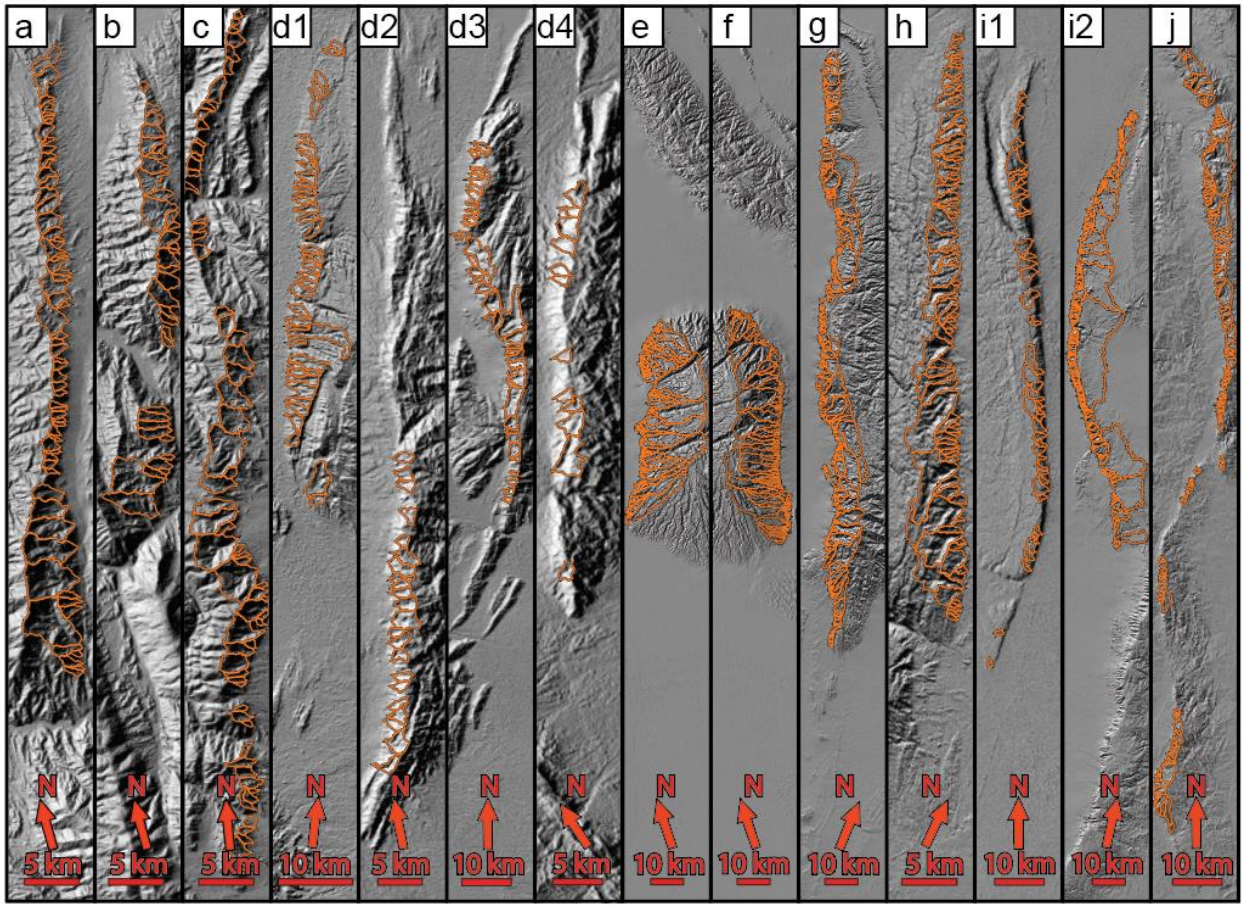

Figure S1. Basin locations. Strip maps of each fault/ fault segment showing the locations of the drainage basin that were measured for various geomorphic indices.

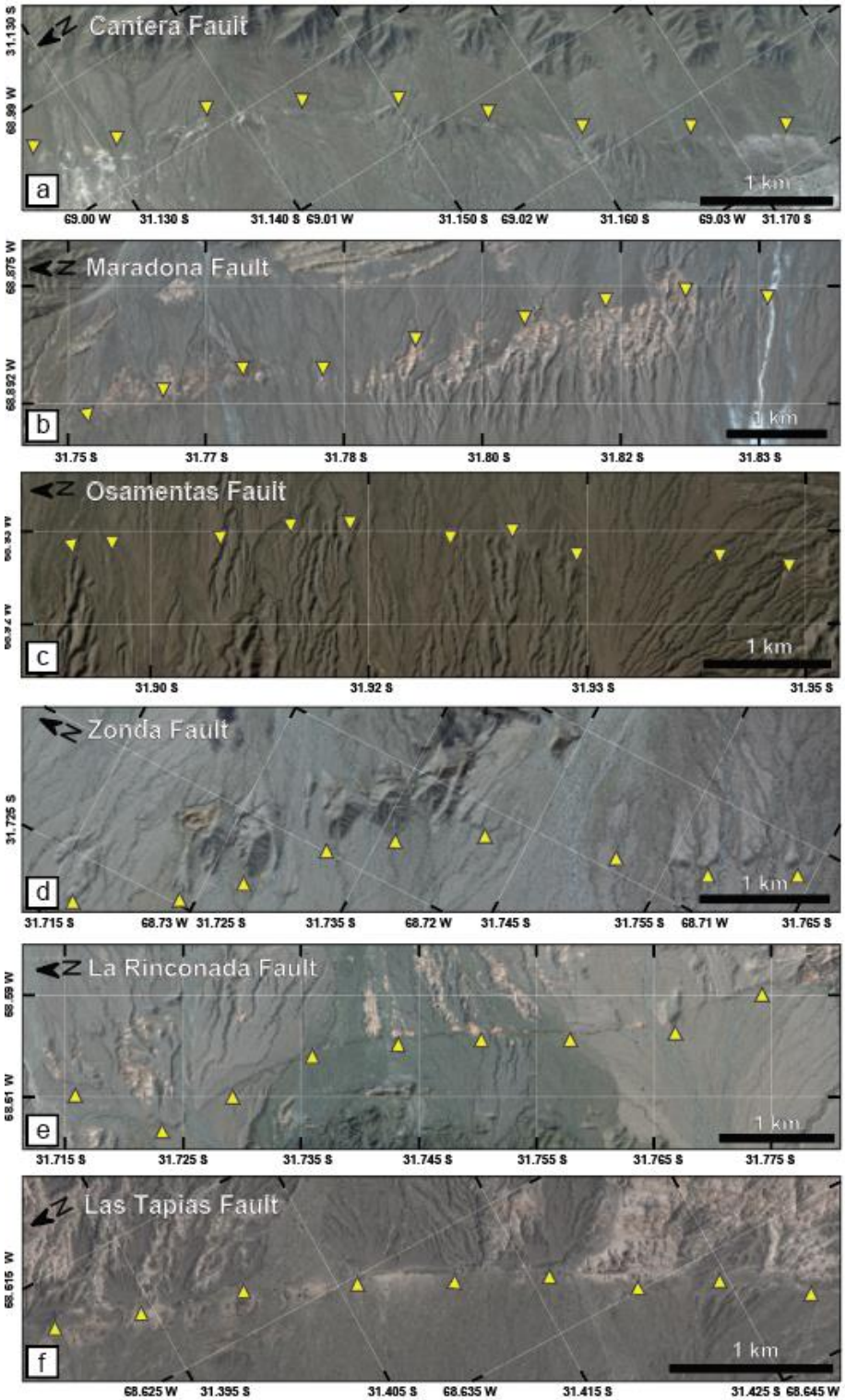

Figure S2. Strip maps showing Quaternary-active scarps associated with the different range-front faults in this study (Part 1). a) Cantera Fault. b) Maradona Fault. c) Osamentas Fault. d) Zonda Fault. e) La Rinconada Fault. f) Las Tapias Fault. Yellow triangles point to the scarp face (copyright Google Earth).

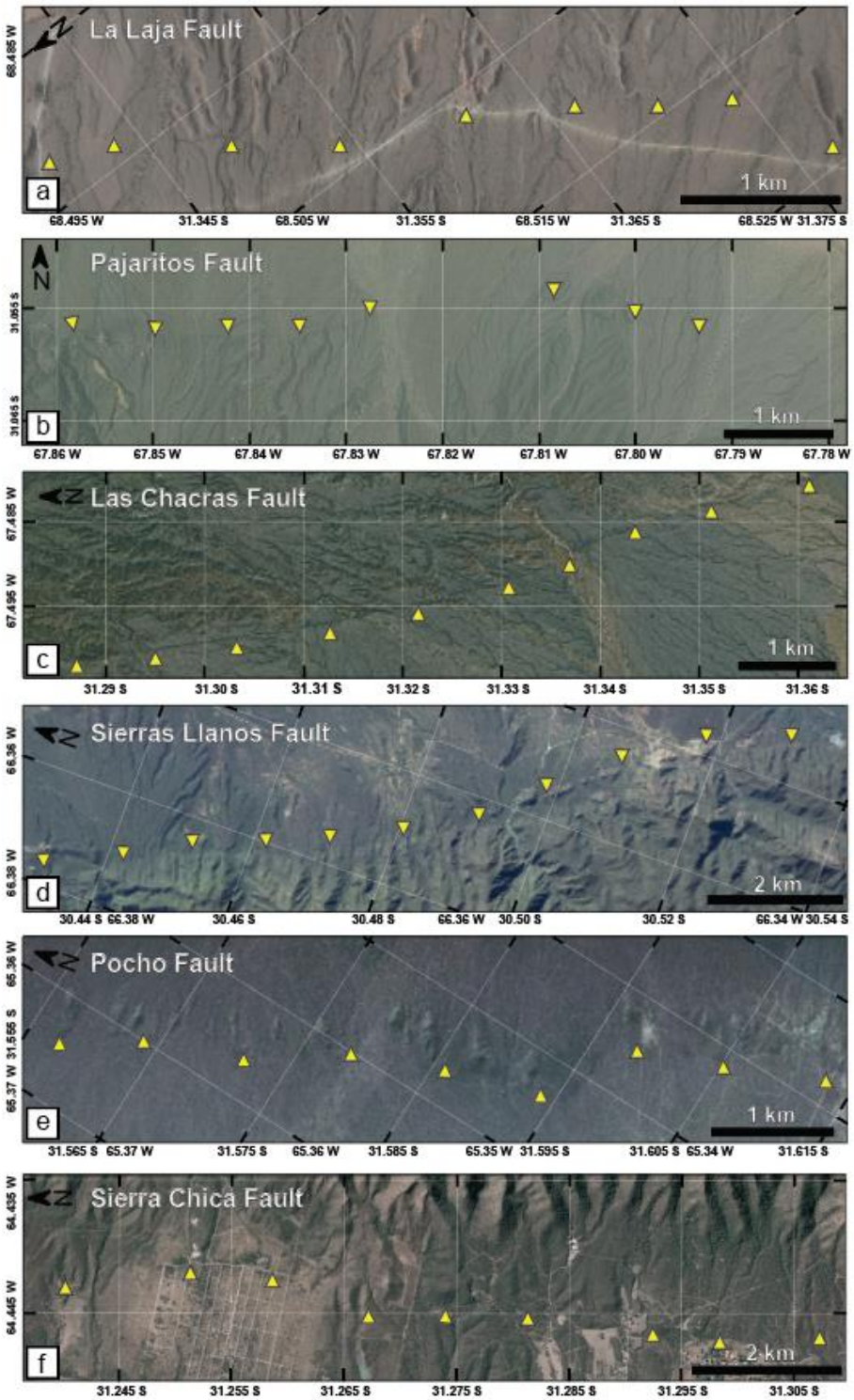

Figure S3. Strip maps showing Quaternary-active scarps associated with the different range-front faults in this study (Part 2). a) La Laja Fault. b) Pajaritos Fault. c) Las Chacras Fault. d) Sierras Llanos Fault. e) Pocho Fault. f) Sierra Chica Fault. Yellow triangles point to the scarp face (copyright Google Earth).

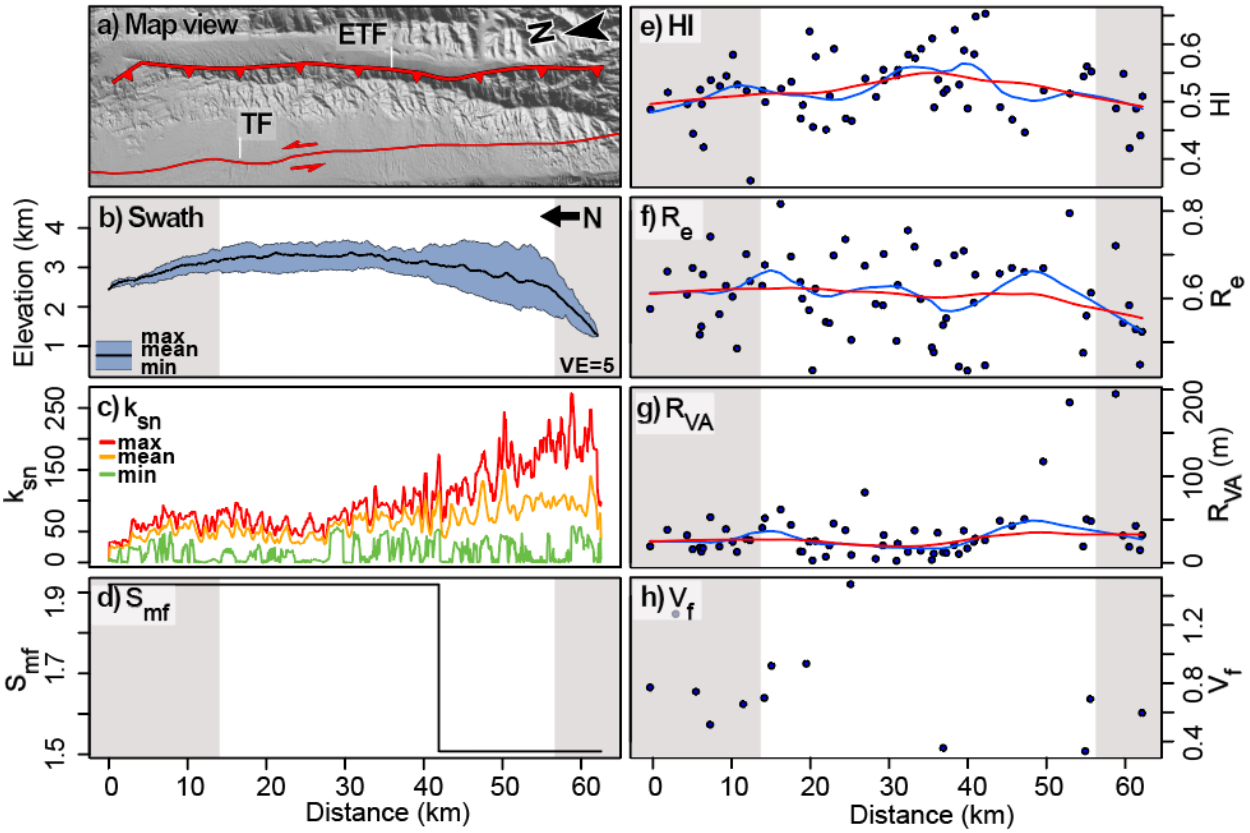

Figure S4. Eastern Sierra del Tigre Fault. a) Map View. ETF—Easter Sierra del Tigre Fault. TF—El Tigre Fault. b) Swath topographic profile. c) K_{sn}. d) S_{mf}. e) HI. f) R_e. g) R_{VA}. h) V_f. The red line and blue lines in graph e, f, and g represent locally weighted regressions with spans of 0.25 and 0.5, respectively. The regions shaded gray are fault tip and fault linkage zones. See Supplementary Fig. S14 for statistical moments of the hypsometric curves for basins inspected in e. See Supplementary Text S2 for full discussion.

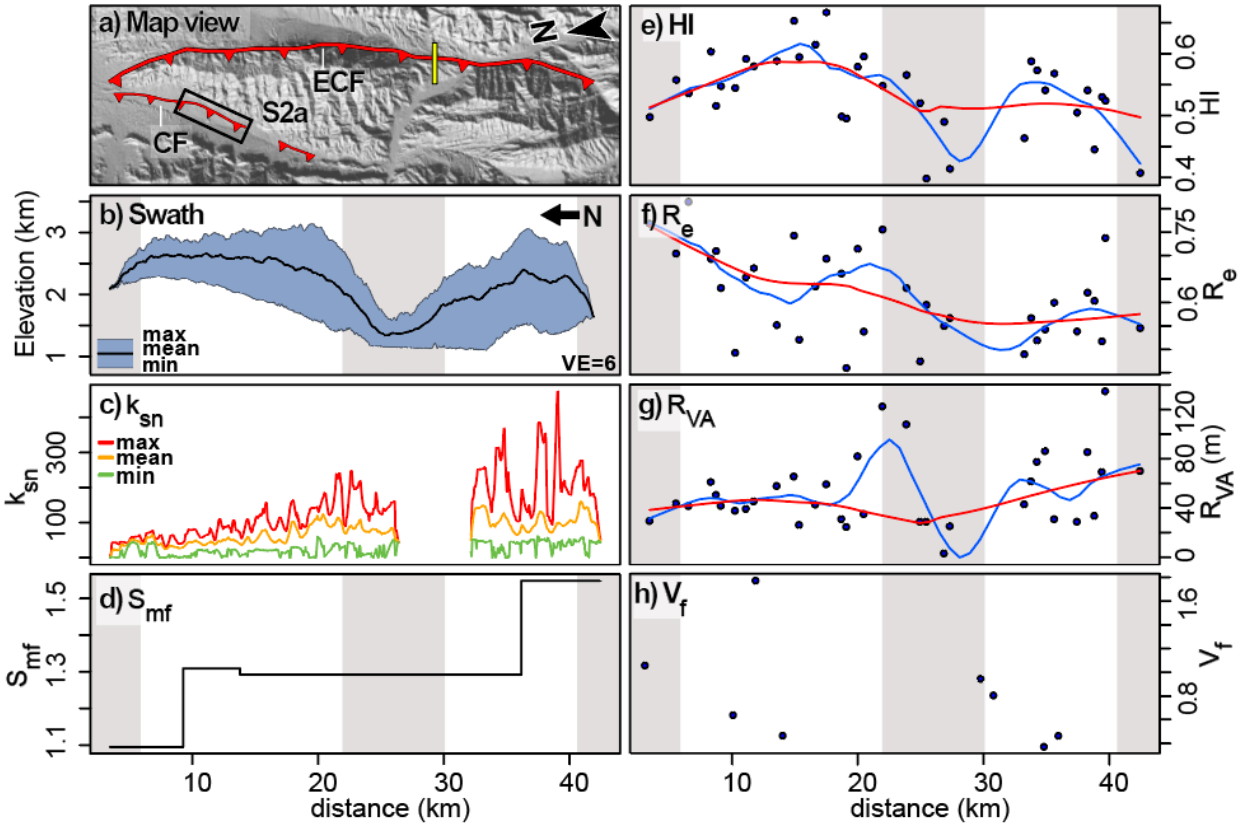

Figure S5. Eastern Sierra de Cantera Fault. a) Map View. CF—La Cantera Fault. ECF—Eastern Sierra de Cantera Fault. Yellow bar indicates fault segment boundaries. Black rectangle indicates the location of Fig. S2a. b) Swath topographic profile. c) K_{sn}. d) S_{mf}. e) HI. f) R_e. g) R_{VA}. h) V_f. The red line and blue lines in graph e, f, and g represent locally weighted regressions with spans of 0.25 and 0.5, respectively. The regions shaded gray are fault tip and fault linkage zones. See Supplementary Fig. S15 for statistical moments of the hypsometric curves for basins inspected in e. See Supplementary Text S3 for full discussion.

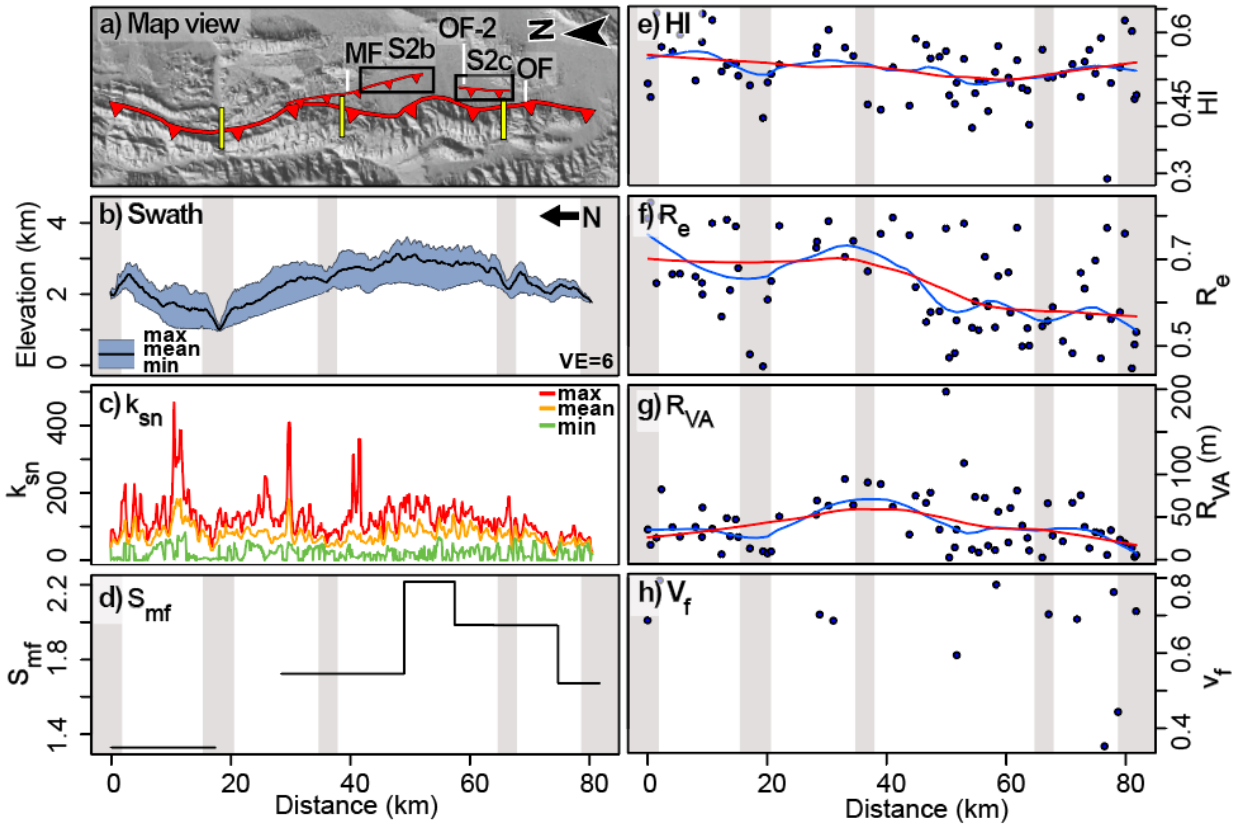

Figure S6. Sierra de Osamentas Fault. a) Map View. MF—Maradona Fault. OF— Sierra de Osamentas Fault. OF-2—Osamentas fault Quaternary-active scarps. Yellow bars indicate fault segment boundaries. Black rectangles indicate the locations of Figs S2b and S2c. b) Swath topographic profile. c) K_{sn}. d) S_{mf}. e) HI. f) R_e. g) R_{VA}. h) V_f. The red line and blue lines in graph e, f, and g represent locally weighted regressions with spans of 0.25 and 0.5, respectively. The regions shaded gray are fault tip and fault linkage zones. See Supplementary Fig. S16 for statistical moments of the hypsometric curves for basins inspected in e. See Supplementary Text S4 for full discussion.

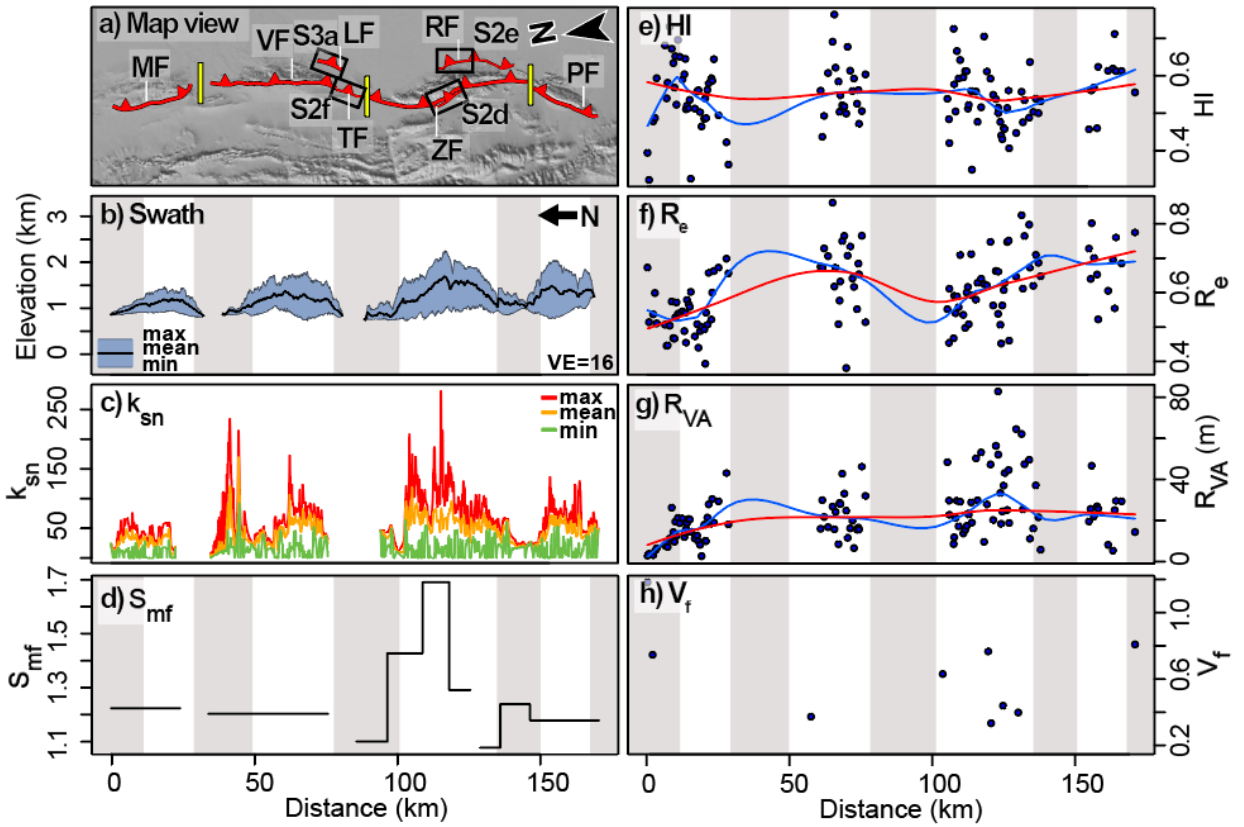

Figure S7. Morados-Villicum-Zonda-Pedernal Faults. a) Map View. MF—Morados Fault. VF—Villicum Fault. TF—Las Tapias Fault. ZF—Zonda Fault. RF—La Rinconada Fault. PF—Pedernal Fault. LF—La Laja Fault. Yellow bars indicate fault segment boundaries. Black rectangles indicate the locations of Figs. S2d-f and S3a. b) Swath topographic profile. c) K_{sn}. d) S_{mf}. e) HI. f) R_e. g) R_{VA}. h) V_f. The red line and blue lines in graph e, f, and g represent locally weighted regressions with spans of 0.25 and 0.5, respectively. The regions shaded gray are fault tip and fault linkage zones. See Supplementary Fig. S17 for statistical moments of the hypsometric curves for basins inspected in e. See Supplementary Text S5 for full discussion.

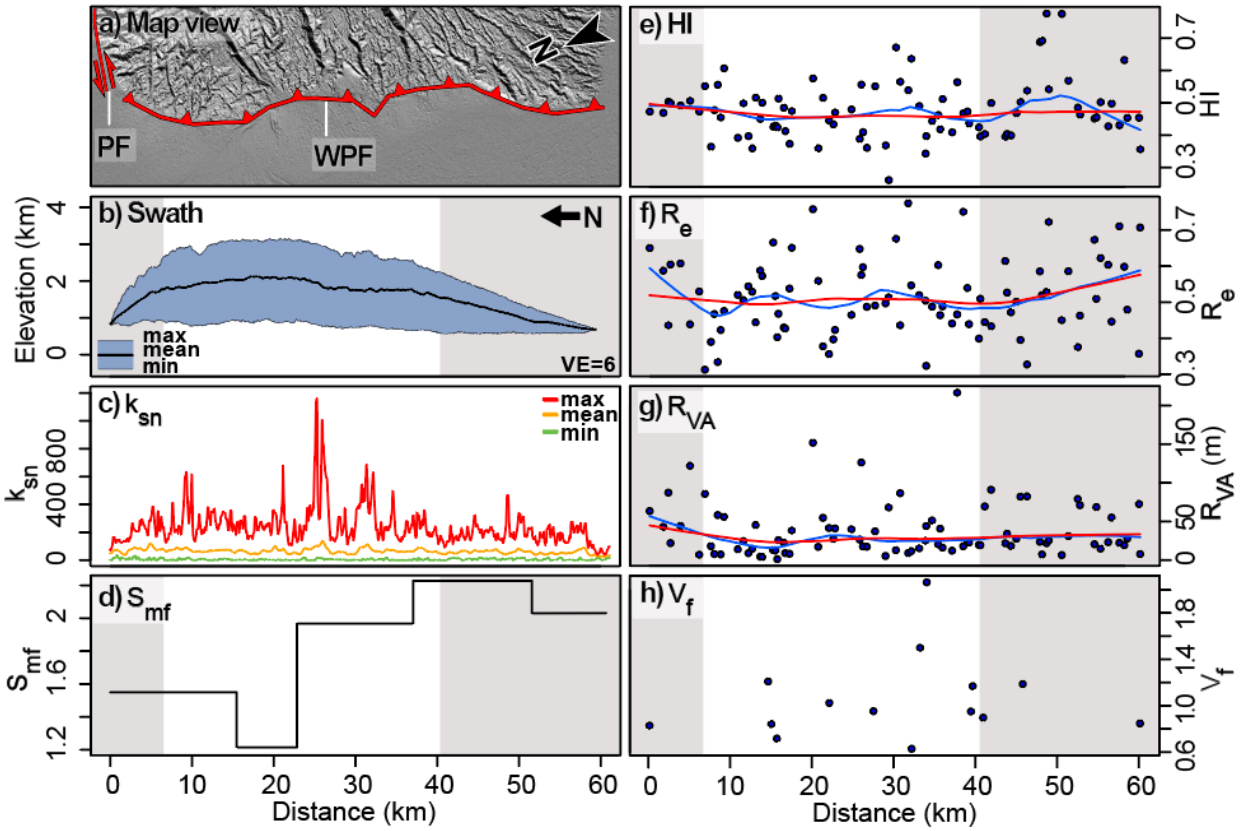

Figure S8. Western Pie de Palo Fault. a) Map View. PF—Pajaritos Fault. WPF— Western Pie de Palo Fault. b) Swath topographic profile. c) K_{sn}. d) S_{mf}. e) HI. f) R_e. g) R_{VA}. h) V_f. The red line and blue lines in graph e, f, and g represent locally weighted regressions with spans of 0.25 and 0.5, respectively. The regions shaded gray are fault tip and fault linkage zones. See Supplementary Fig. S18 for statistical moments of the hypsometric curves for basins inspected in e. See Supplementary Text S6 for full discussion.

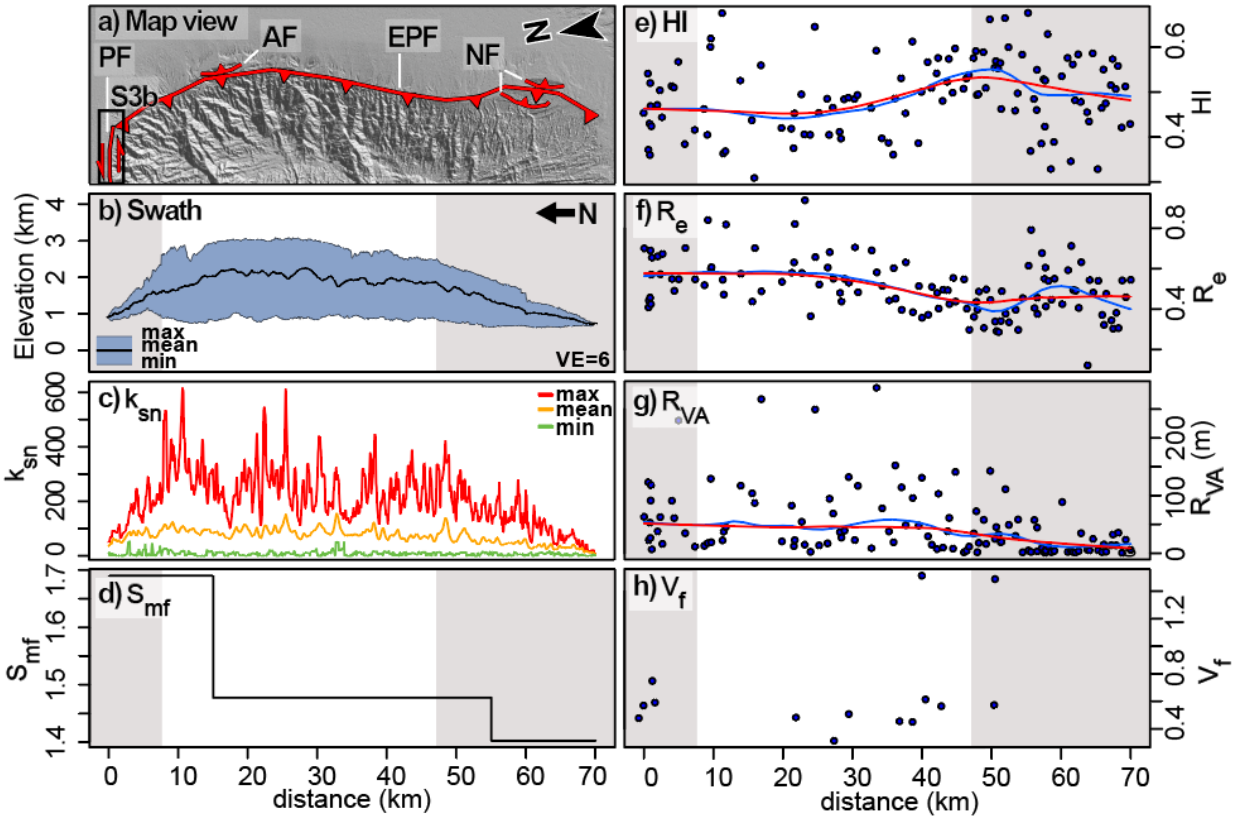

Figure S9. Eastern Pie de Palo Fault. a) Map View. PF—Pajaritos Fault. EPF—Eastern Pie de Palo Fault. AF—Ampacama Fault. NF—Niquizanga Fault. Black rectangle indicates the location of Fig. S3b. b) Swath topographic profile. c) K_{sn}. d) S_{mf}. e) HI. f) R_e. g) R_{VA}. h) V_f. The red line and blue lines in graph e, f, and g represent locally weighted regressions with spans of 0.25 and 0.5, respectively. The regions shaded gray are fault tip and fault linkage zones. See Supplementary Fig. S19 for statistical moments of the hypsometric curves for basins inspected in e. See Supplementary Text S7 for full discussion.

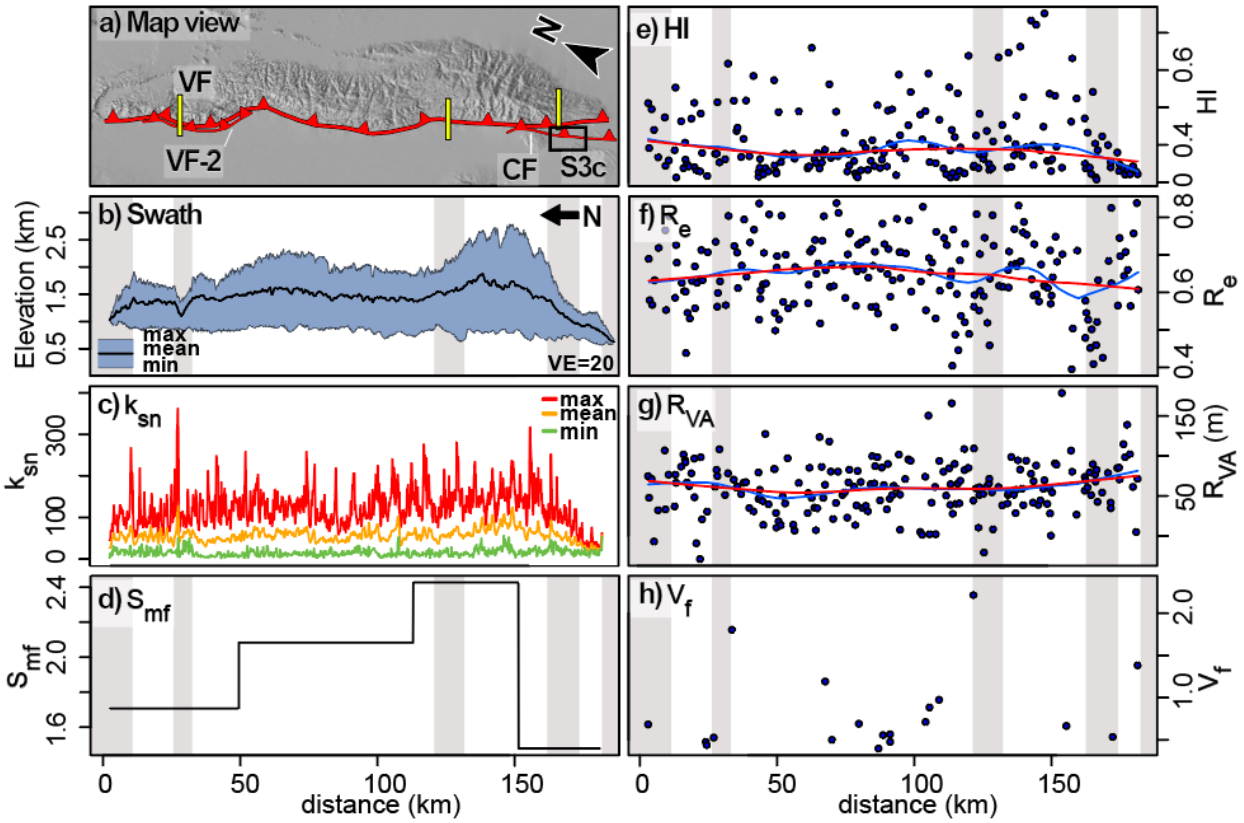

Figure S10. Valle Fertil Fault. a) Map View. VF— Valle Fertil Fault. VF-2— Valle Fertil Fault Quaternary-active scarps. CF— Las Chacras Fault. Yellow bar/s indicates fault segment boundaries. Black rectangle indicates the location of Fig. S3c. b) Swath topographic profile. c) K_{sn}. d) S_{mf}. e) HI. f) R_e. g) R_{VA}. h) V_f. The red line and blue lines in graph e, f, and g represent locally weighted regressions with spans of 0.25 and 0.5, respectively. The regions shaded gray are fault tip and fault linkage zones. See Supplementary Fig. S20 for statistical moments of the hypsometric curves for basins inspected in e. See Supplementary Text S8 for full discussion.

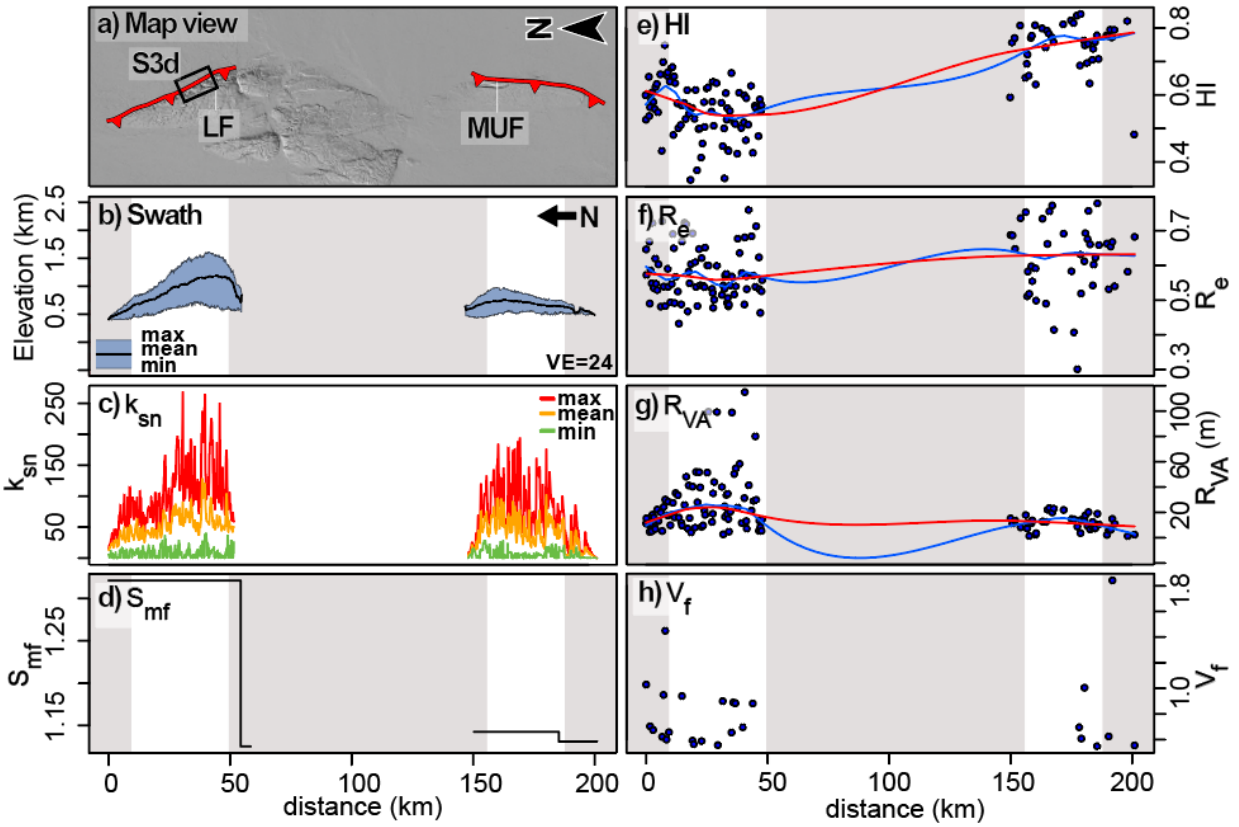

Figure S11. Sierra de los Llanos and Sierra de las Minas y Ulapes Fault. a) Map View. LF—Sierra de los Llanos Fault. MUF—Sierra Minas y Ulapes Fault. Black rectangle indicates the location of Fig. S3d. b) Swath topographic profile. c) K_{sn}. d) S_{mf}. e) HI. f) R_e. g) R_{VA}. h) V_f. The red line and blue lines in graph e, f, and g represent locally weighted regressions with spans of 0.25 and 0.5, respectively. The regions shaded gray are fault tip and fault linkage zones. See Supplementary Fig. S21 for statistical moments of the hypsometric curves for basins inspected in e. See Supplementary Text S9 for full discussion.

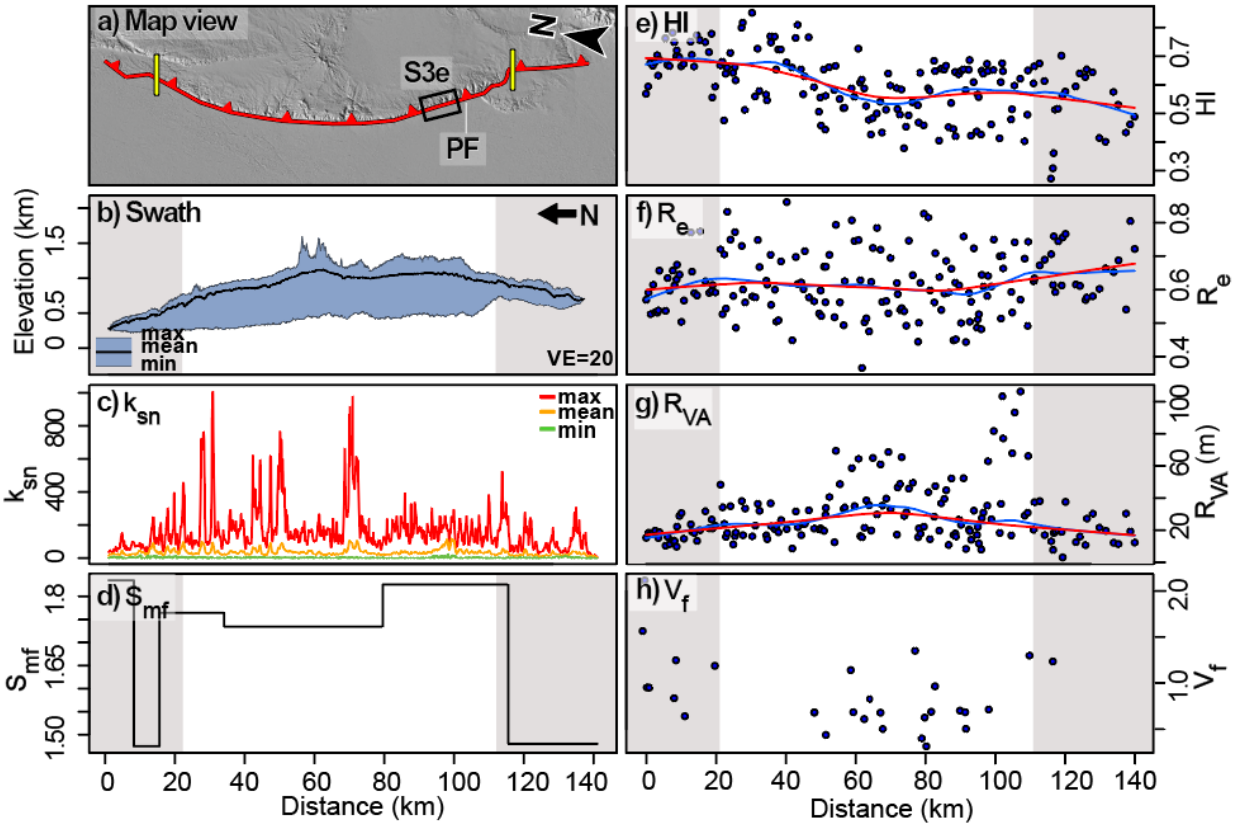

Figure S12. Pocho Fault. a) Map View. PF—Pocho Fault. Yellow bar/s indicates fault segment boundaries. Black rectangle indicates the location of Fig. S3e. b) Swath topographic profile. c) K_{sn}. d) S_{mf}. e) HI. f) R_e. g) R_{VA}. h) V_f. The red line and blue lines in graph e, f, and g represent locally weighted regressions with spans of 0.25 and 0.5, respectively. The regions shaded gray are fault tip and fault linkage zones. See Supplementary Fig. S22 for statistical moments of the hypsometric curves for basins inspected in e. See Supplementary Text S10 for full discussion.

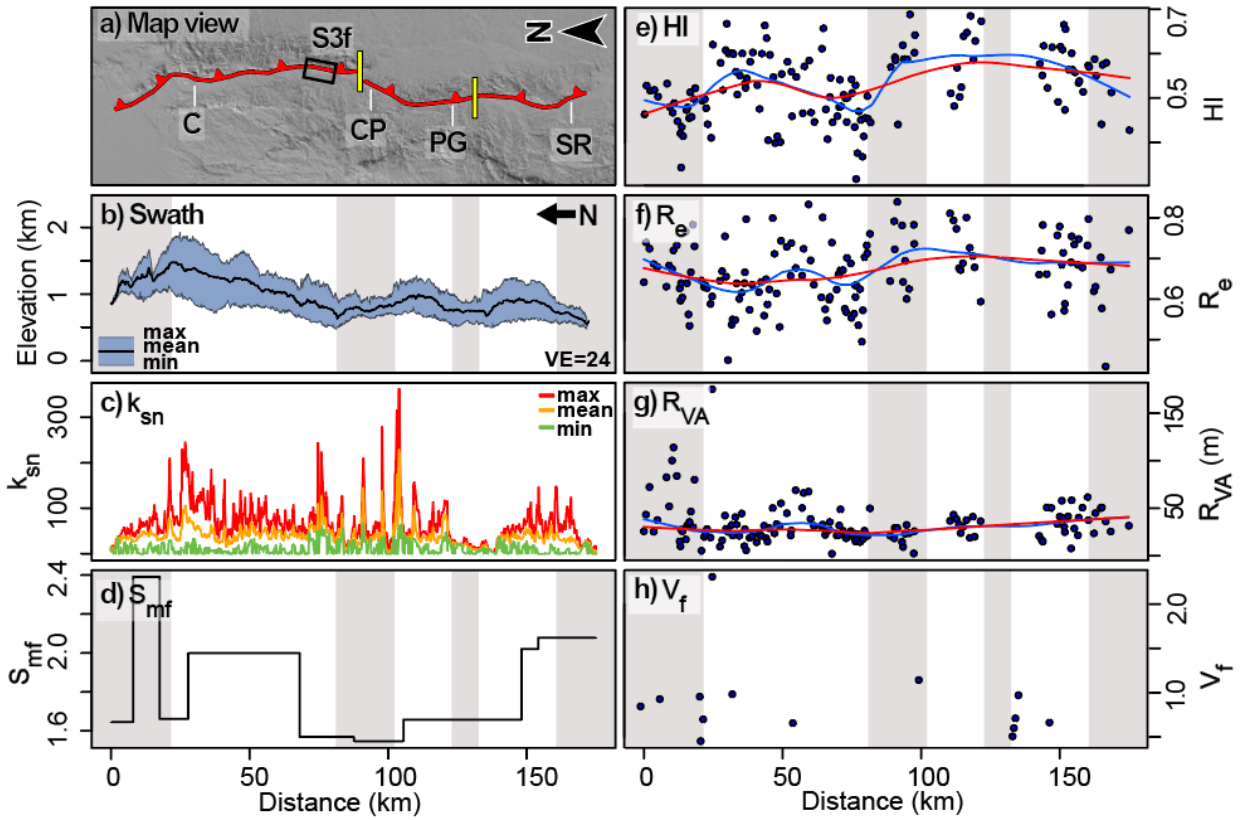

Figure S13. Sierra Chica Fault Zone. a) Map View. C—Cosquin Fault. CP—Carlos Paz Fault. PG—Potrero de Garay Fault. SR—Santa Rosa Fault. Yellow bar/s indicates fault segment boundaries. Black rectangle indicates the location of Fig. S3f. b) Swath topographic profile. c) K_{sn}. d) S_{mf}. e) HI. f) R_e. g) R_{VA}. h) V_f. The red line and blue lines in graph e, f, and g represent locally weighted regressions with spans of 0.25 and 0.5, respectively. The regions shaded gray are fault tip and fault linkage zones. See Supplementary Fig. S23 for statistical moments of the hypsometric curves for basins inspected in e. See Supplementary Text S11 for full discussion.

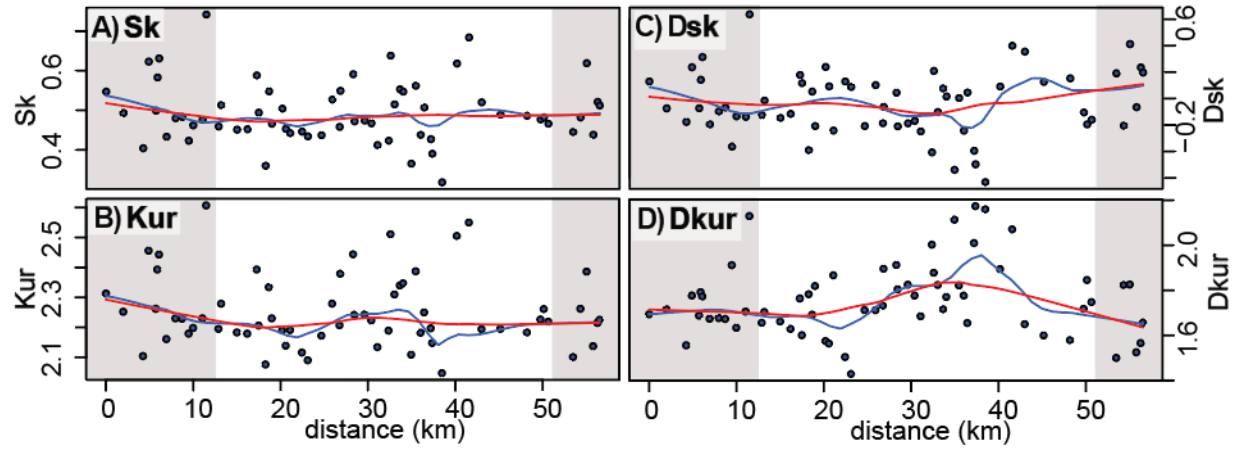

Figure S14. Eastern Sierra del Tigre Fault. A) Skewness (Sk). B) Kurtosis (Kur). C) Density Skewness (Dsk). D) Density Kurtosis (Dkur). The red line and blue lines represent locally weighted regressions with spans of 0.25 and 0.5, respectively. The regions shaded gray are fault tip and/or fault linkage zones.

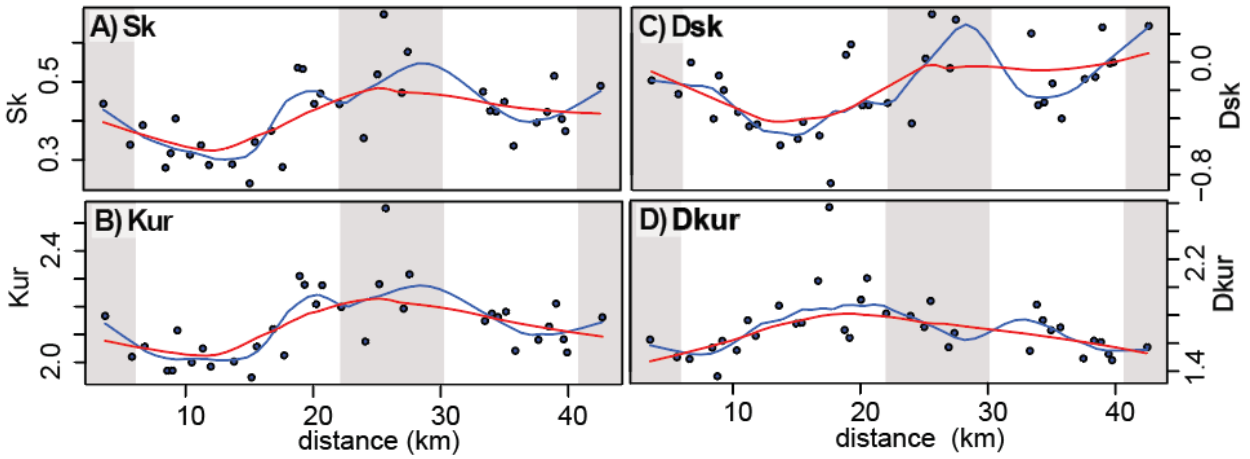

Figure S15. Eastern Sierra de Cantera Fault. A) Skewness (Sk). B) Kurtosis (Kur). C) Density Skewness (Dsk). D) Density Kurtosis (Dkur). The red line and blue lines represent locally weighted regressions with spans of 0.25 and 0.5, respectively. The regions shaded gray are fault tip and/or fault linkage zones.

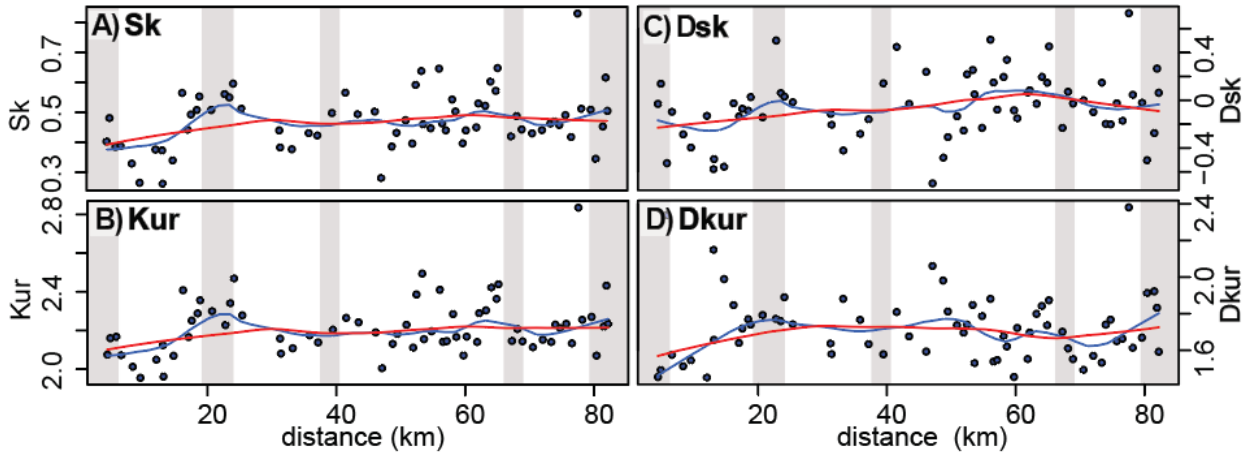

Figure S16. Sierra de Osamentas Fault. A) Skewness (Sk). B) Kurtosis (Kur). C) Density Skewness (Dsk). D) Density Kurtosis (Dkur). The red line and blue lines represent locally weighted regressions with spans of 0.25 and 0.5, respectively. The regions shaded gray are fault tip and/or fault linkage zones.

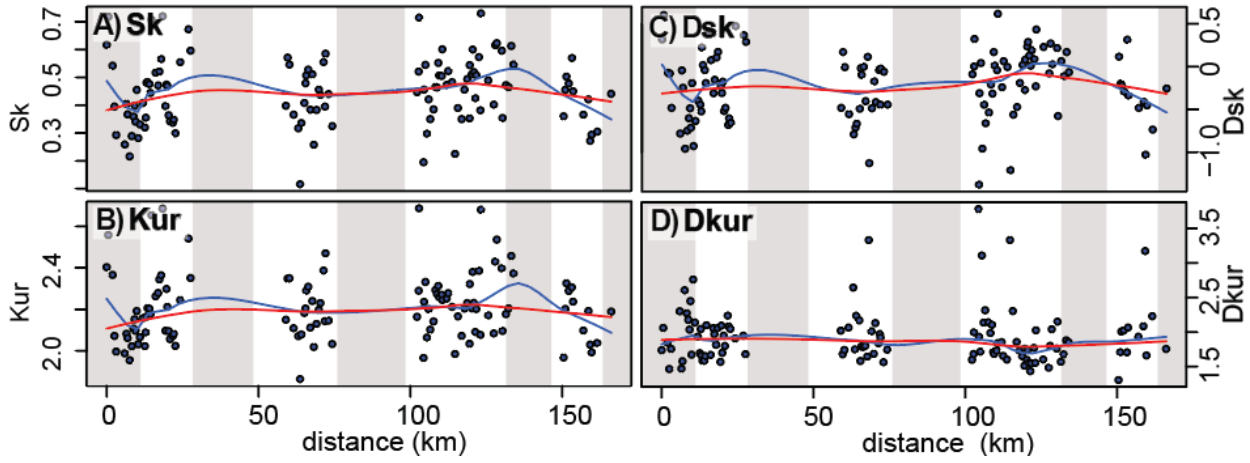

Figure S17. Morados-Villicum-Zonda-Pedernal Faults. A) Skewness (Sk). B) Kurtosis (Kur). C) Density

Skewness (Dsk). D) Density Kurtosis (Dkur). The red line and blue lines represent locally weighted regressions with spans of 0.25 and 0.5, respectively. The regions shaded gray are fault tip and/or fault linkage zones.

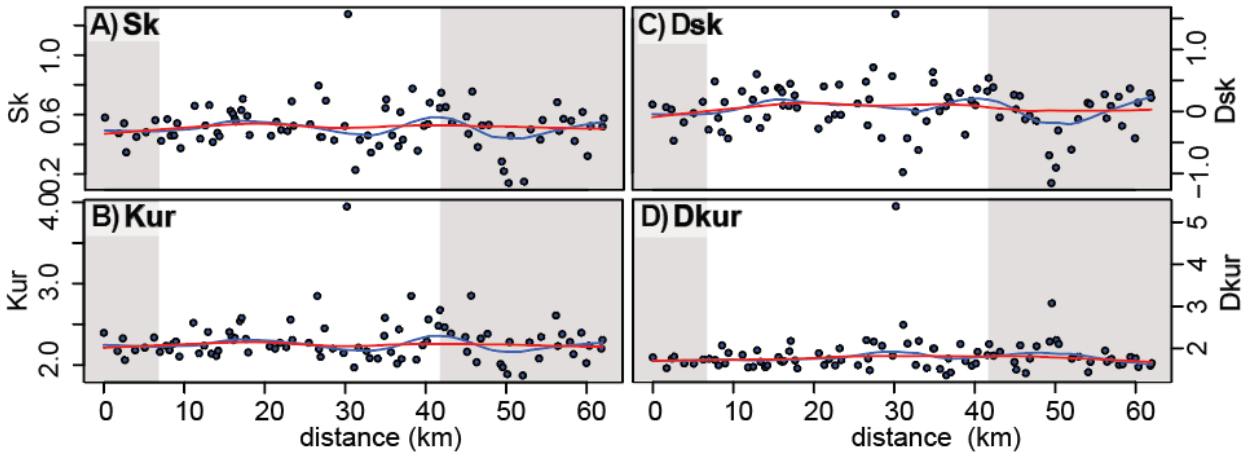

Figure S18. Western Pie de Palo Fault. A) Skewness (Sk). B) Kurtosis (Kur). C) Density Skewness (Dsk). D) Density Kurtosis (Dkur). The red line and blue lines represent locally weighted regressions with spans of 0.25 and 0.5, respectively. The regions shaded gray are fault tip and/or fault linkage zones.

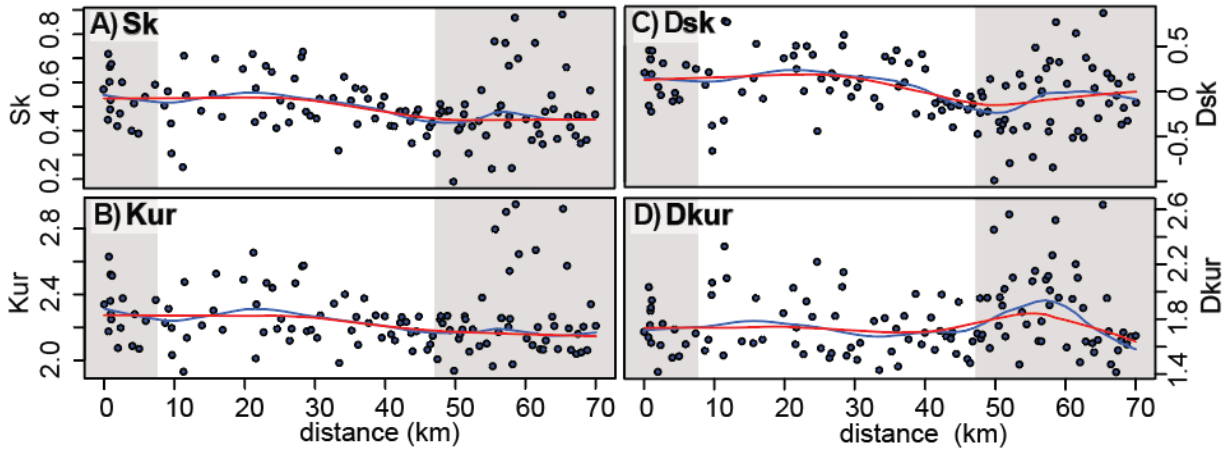

Figure S19. Eastern Pie de Palo Fault. A) Skewness (Sk). B) Kurtosis (Kur). C) Density Skewness (Dsk). D) Density Kurtosis (Dkur). The red line and blue lines represent locally weighted regressions with spans of 0.25 and 0.5, respectively. The regions shaded gray are fault tip and/or fault linkage zones.

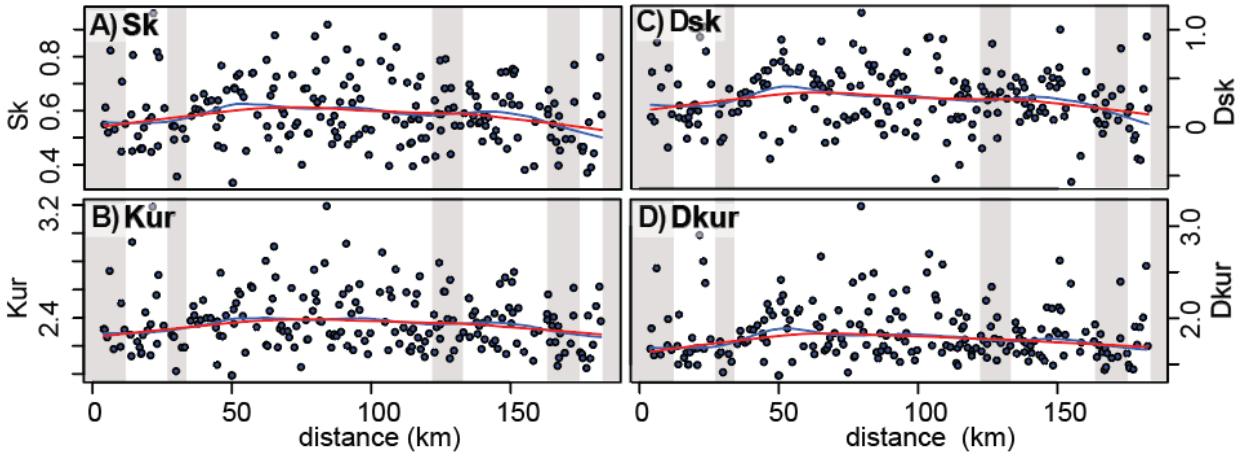

Figure S20. Valle Fertil Fault. A) Skewness (Sk). B) Kurtosis (Kur). C) Density Skewness (Dsk). D) Density Kurtosis (Dkur). The red line and blue lines represent locally weighted regressions with spans of 0.25 and 0.5, respectively. The regions shaded gray are fault tip and/or fault linkage zones.

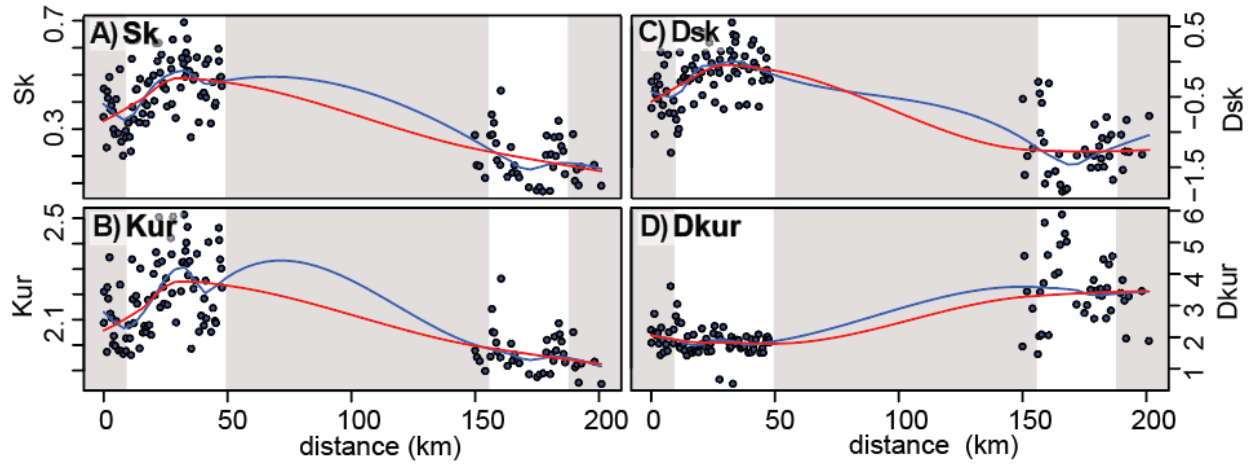

Figure S21. Sierra de los Llanos and Sierra de las Minas y Ulapes Fault. A) Skewness (Sk). B) Kurtosis (Kur). C) Density Skewness (Dsk). D) Density Kurtosis (Dkur). The red line and blue lines represent locally weighted regressions with spans of 0.25 and 0.5, respectively. The regions shaded gray are fault tip and/or fault linkage zones.

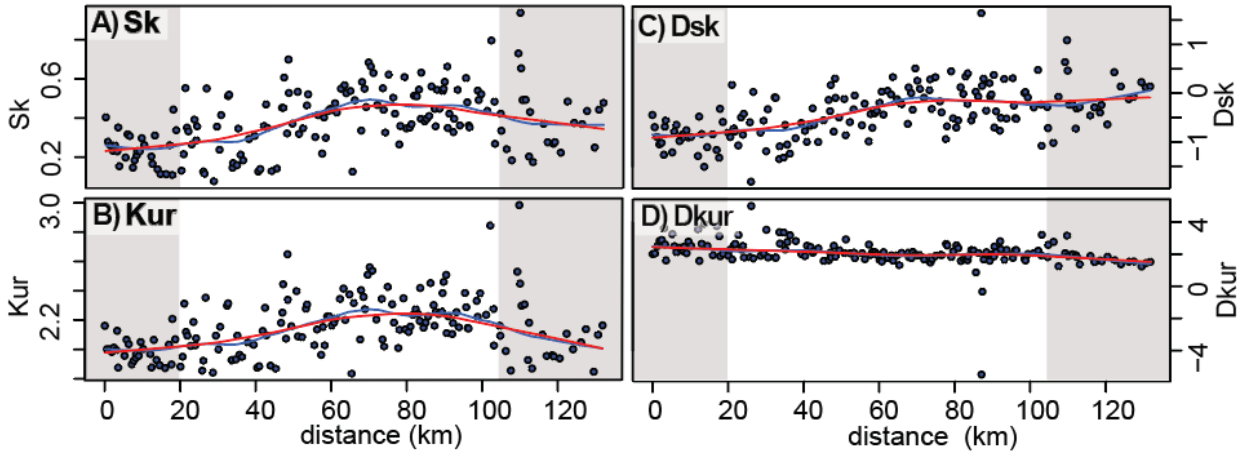

Figure S22. Pocho Fault. A) Skewness (Sk). B) Kurtosis (Kur). C) Density Skewness (Dsk). D) Density Kurtosis (Dkur). The red line and blue lines represent locally weighted regressions with spans of 0.25 and 0.5, respectively. The regions shaded gray are fault tip and/or fault linkage zones.

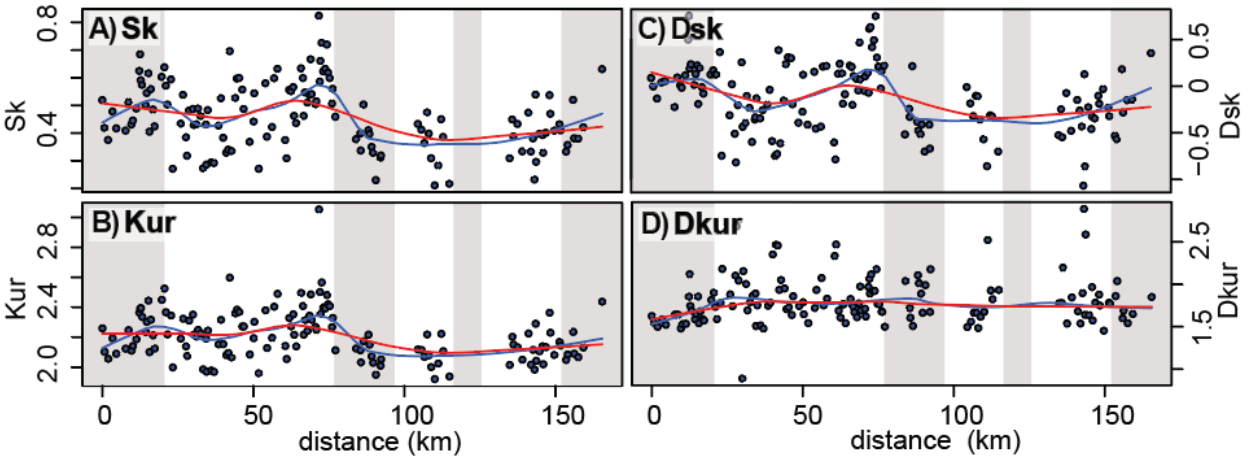

Figure S23. Sierra Chica Fault Zone. A) Skewness (Sk). B) Kurtosis (Kur). C) Density Skewness (Dsk). D) Density Kurtosis (Dkur). The red line and blue lines represent locally weighted regressions with spans of 0.25 and 0.5, respectively. The regions shaded gray are fault tip and/or fault linkage zones.

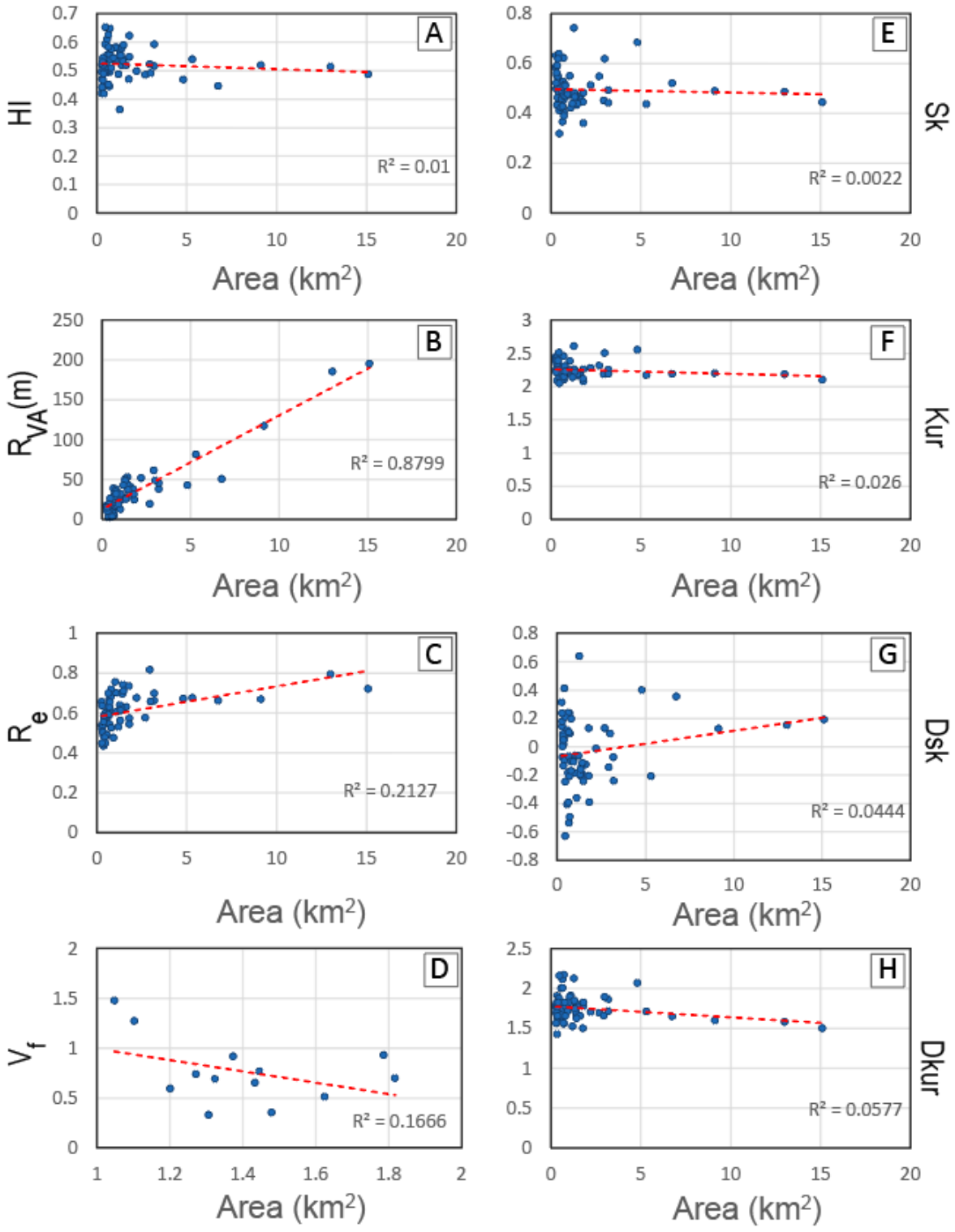

Figure S24. Geomorphic indices vs. area correlation graphs for Eastern Sierra del Tigre Fault. A) Hypsometric Integral (HI). B) Volume-to-Area Ratio (R_{VA}). C) Basin Elongation Ratio (R_e). D) Valley floor width-to-height Ratio (V_f). E) Skewness (Sk). F) Kurtosis (Kur). G) Density Skewness (Dsk). H) Density Kurtosis (Dkur).

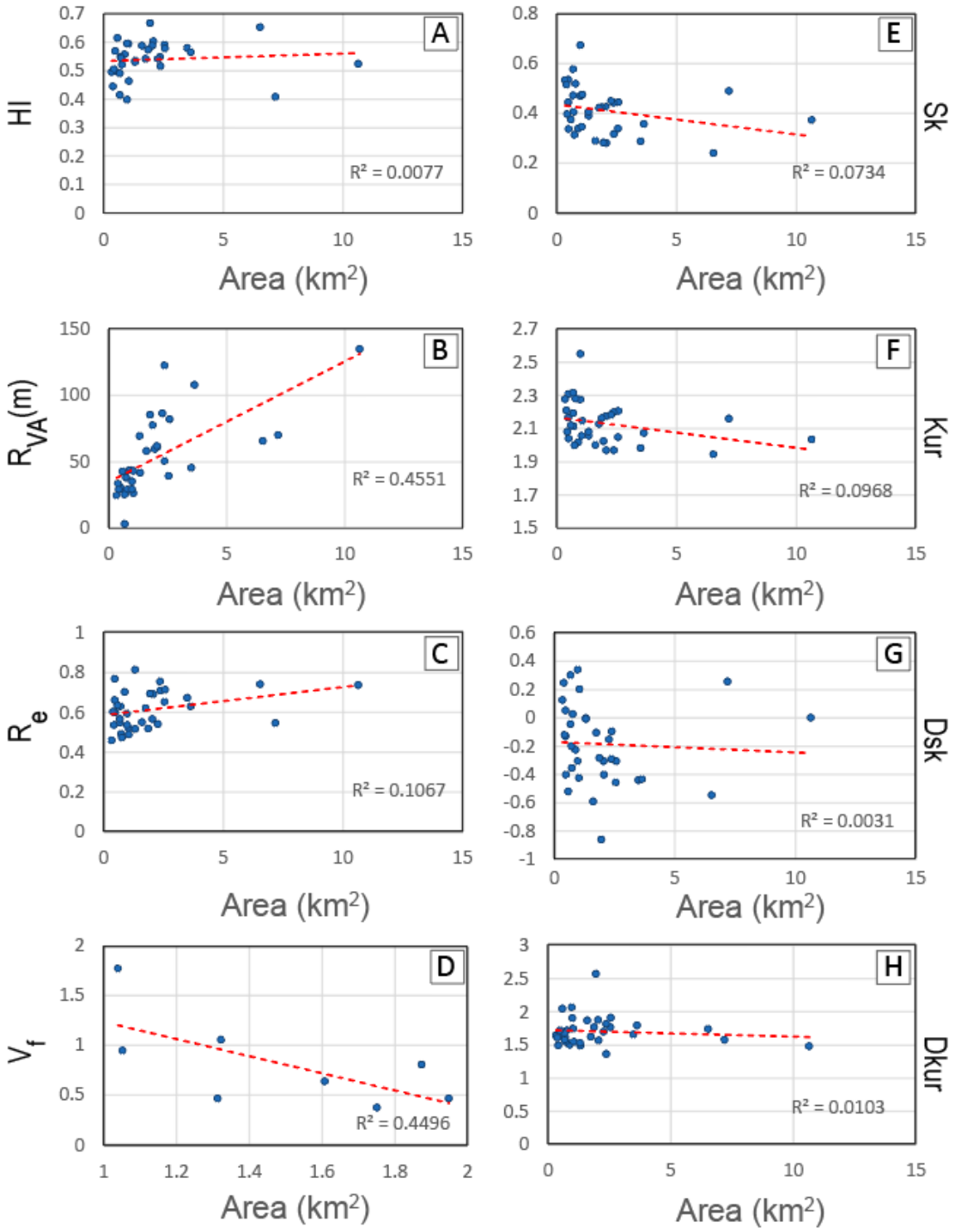

Figure S25. Geomorphic indices vs. area correlation graphs for Eastern Sierra de Cantera Fault. A) Hypsometric Integral (HI). B) Volume-to-Area Ratio (R_{VA}). C) Basin Elongation Ratio (R_e). D) Valley floor width-to-height Ratio (V_f). E) Skewness (Sk). F) Kurtosis (Kur). G) Density Skewness (Dsk). H) Density Kurtosis (Dkur).

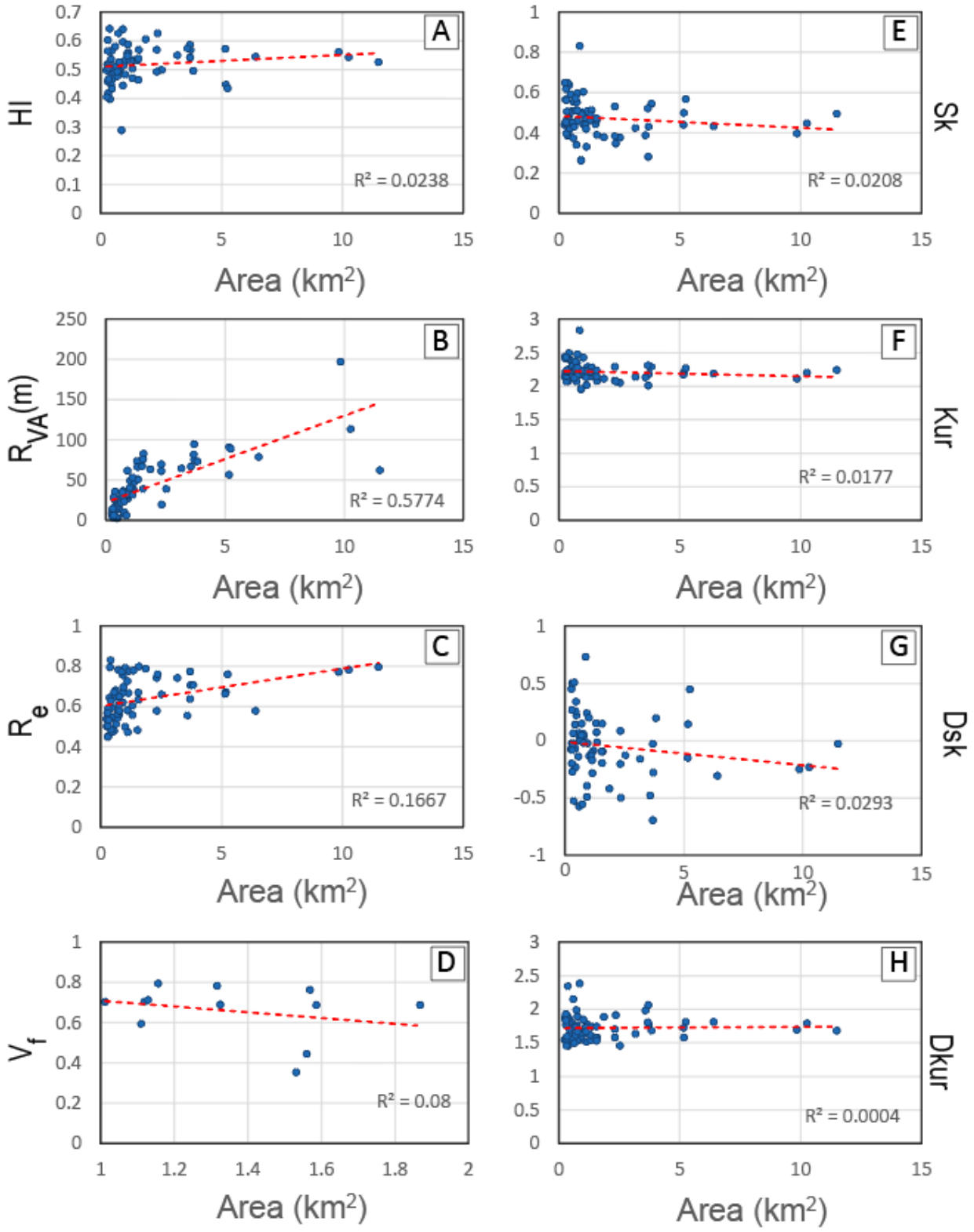

Figure S26. Geomorphic indices vs. area correlation graphs for Sierra de Osamentas Fault. A) Hypsometric Integral (HI). B) Volume-to-Area Ratio (R_{VA}). C) Basin Elongation Ratio (R_e). D) Valley floor width-to-height Ratio (V_f). E) Skewness (Sk). F) Kurtosis (Kur). G) Density Skewness (Dsk). H) Density Kurtosis (Dkur).

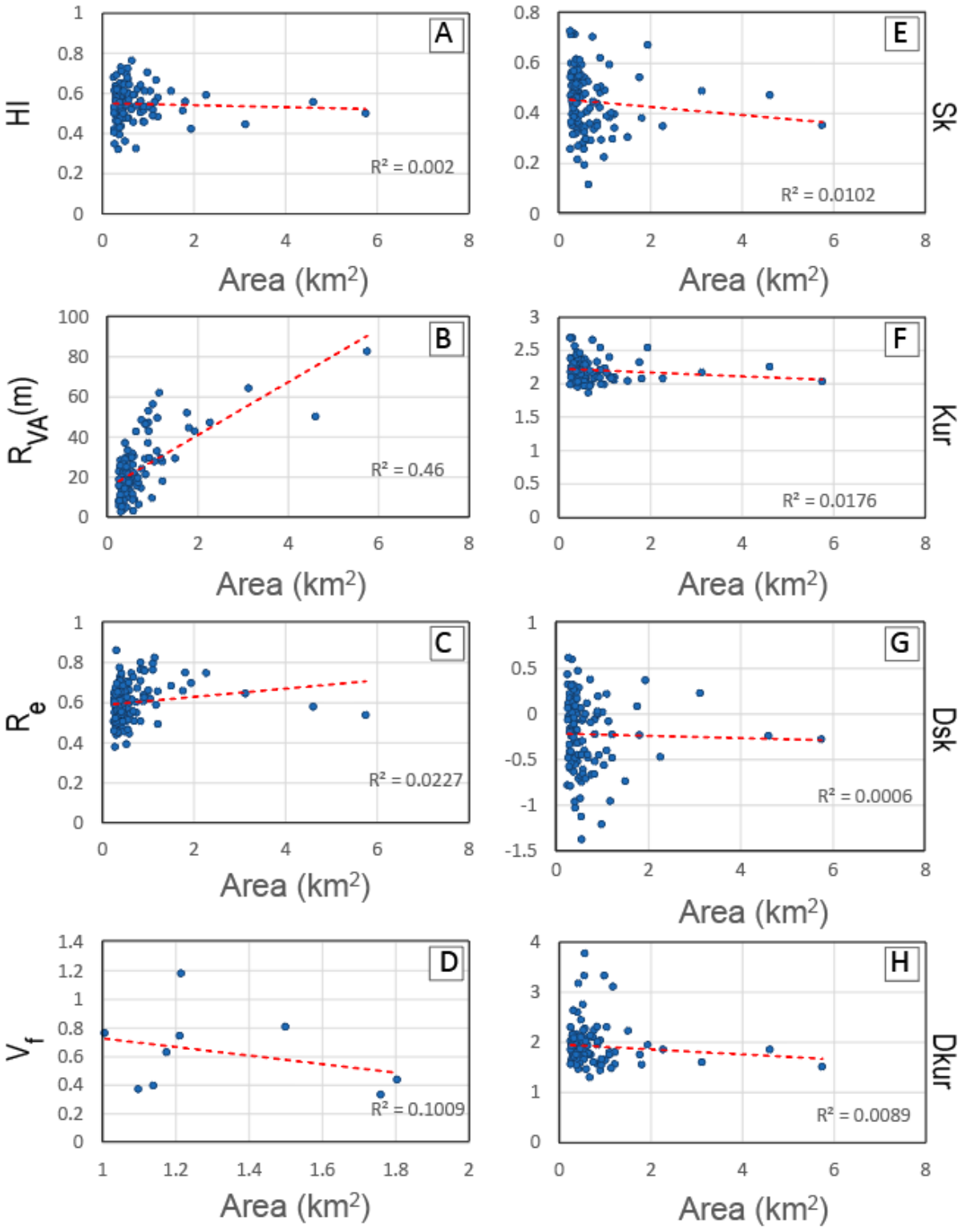

Figure S27. Geomorphic indices vs. area correlation graphs for Morados-Villicum-Zonda-Pedernal Faults. A) Hypsometric Integral (HI). B) Volume-to-Area Ratio (R_{VA}). C) Basin Elongation Ratio (R_e). D) Valley floor

width-to-height Ratio (V_f). E) Skewness (Sk). F) Kurtosis (Kur). G) Density Skewness (Dsk). H) Density Kurtosis (Dkur).

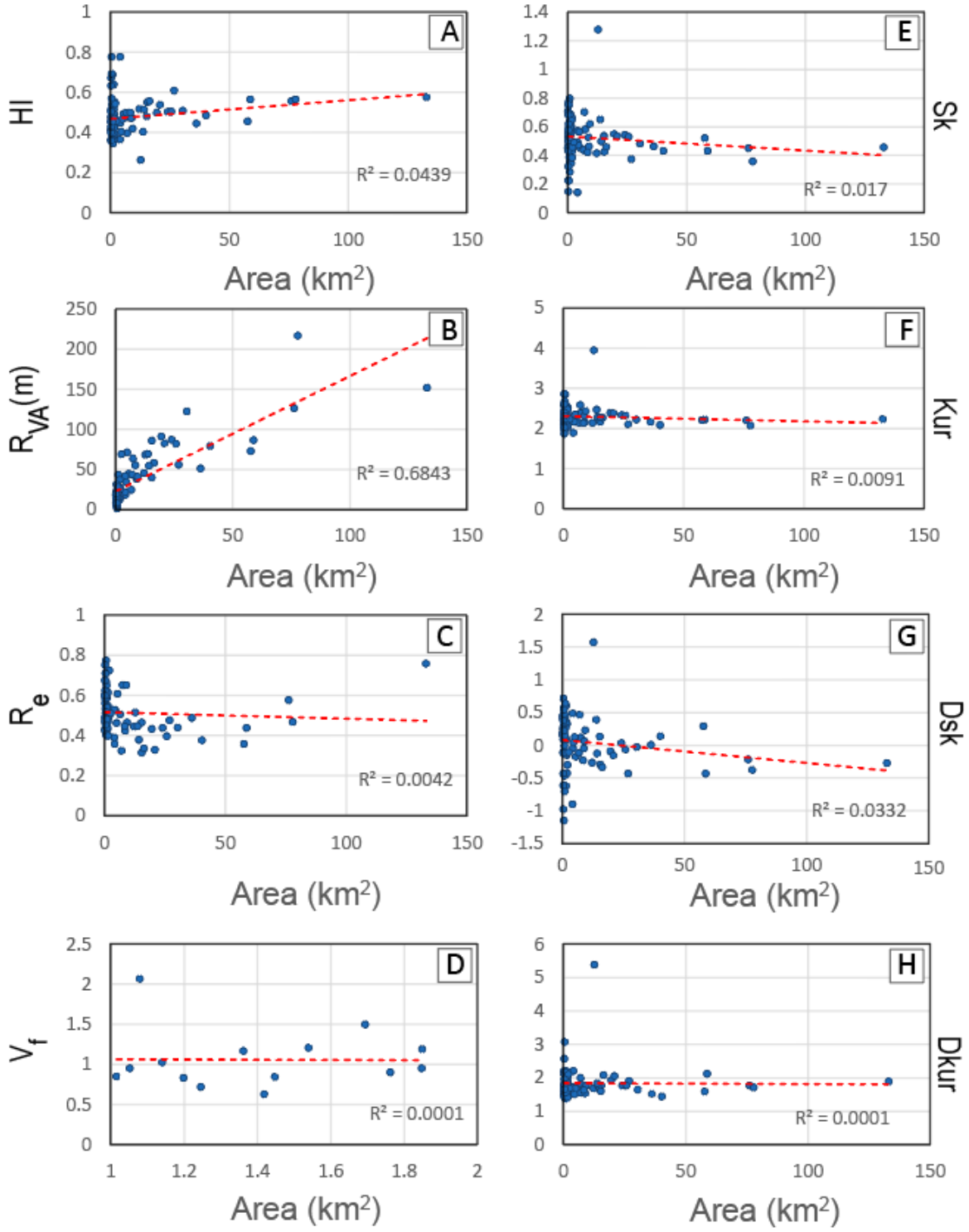

Figure S28. Geomorphic indices vs. area correlation graphs for Western Pie de Palo Fault. A) Hypsometric

Integral (HI). B) Volume-to-Area Ratio (R_{VA}). C) Basin Elongation Ratio (R_e). D) Valley floor width-to-height Ratio (V_f). E) Skewness (Sk). F) Kurtosis (Kur). G) Density Skewness (Dsk). H) Density Kurtosis (Dkur).

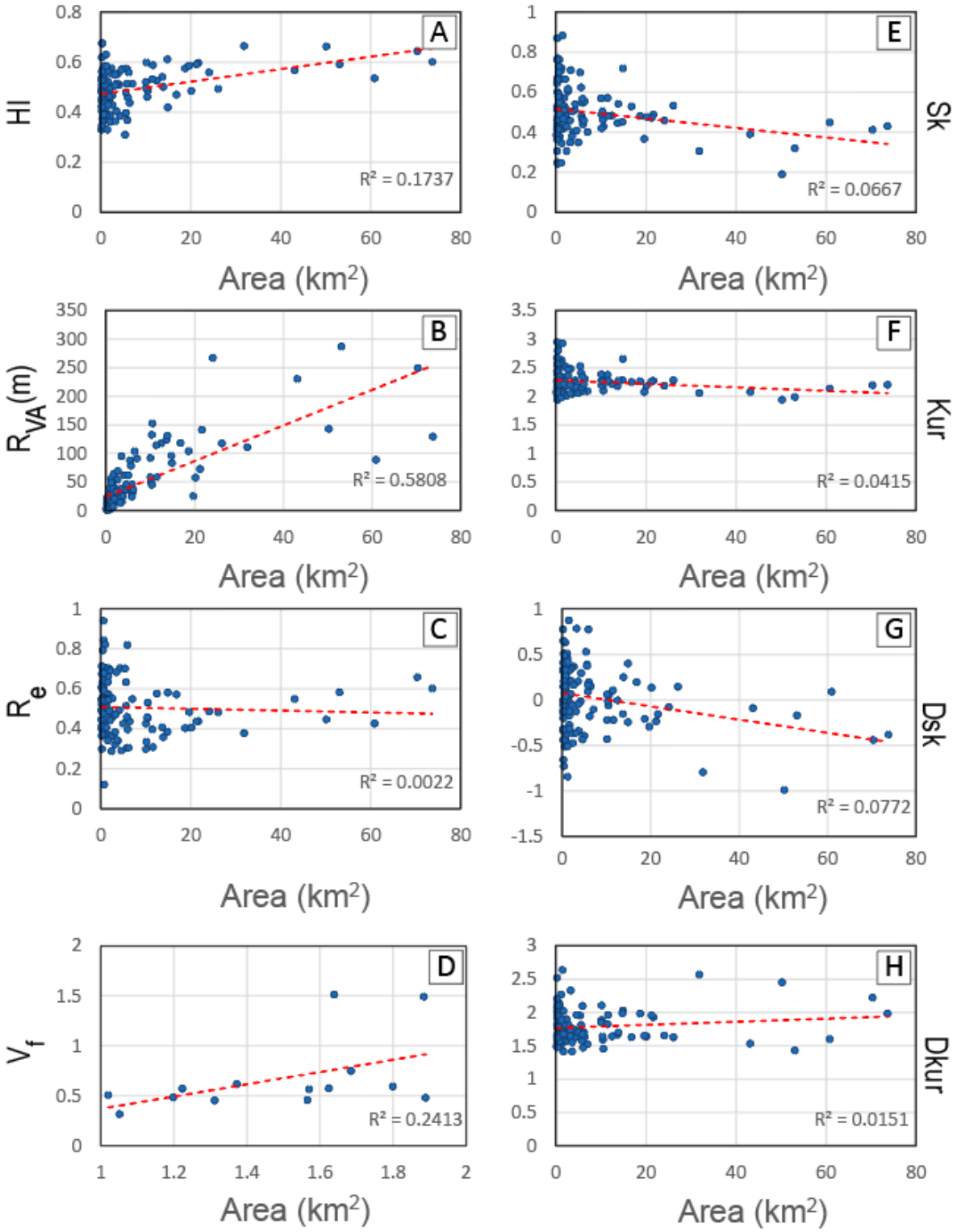

Figure S29. Geomorphic indices vs. area correlation graphs for Eastern Pie de Palo Fault. A) Hypsometric Integral (HI). B) Volume-to-Area Ratio (R_{VA}). C) Basin Elongation Ratio (R_e). D) Valley floor width-to-height Ratio (V_f). E) Skewness (Sk). F) Kurtosis (Kur). G) Density Skewness (Dsk). H) Density Kurtosis (Dkur).

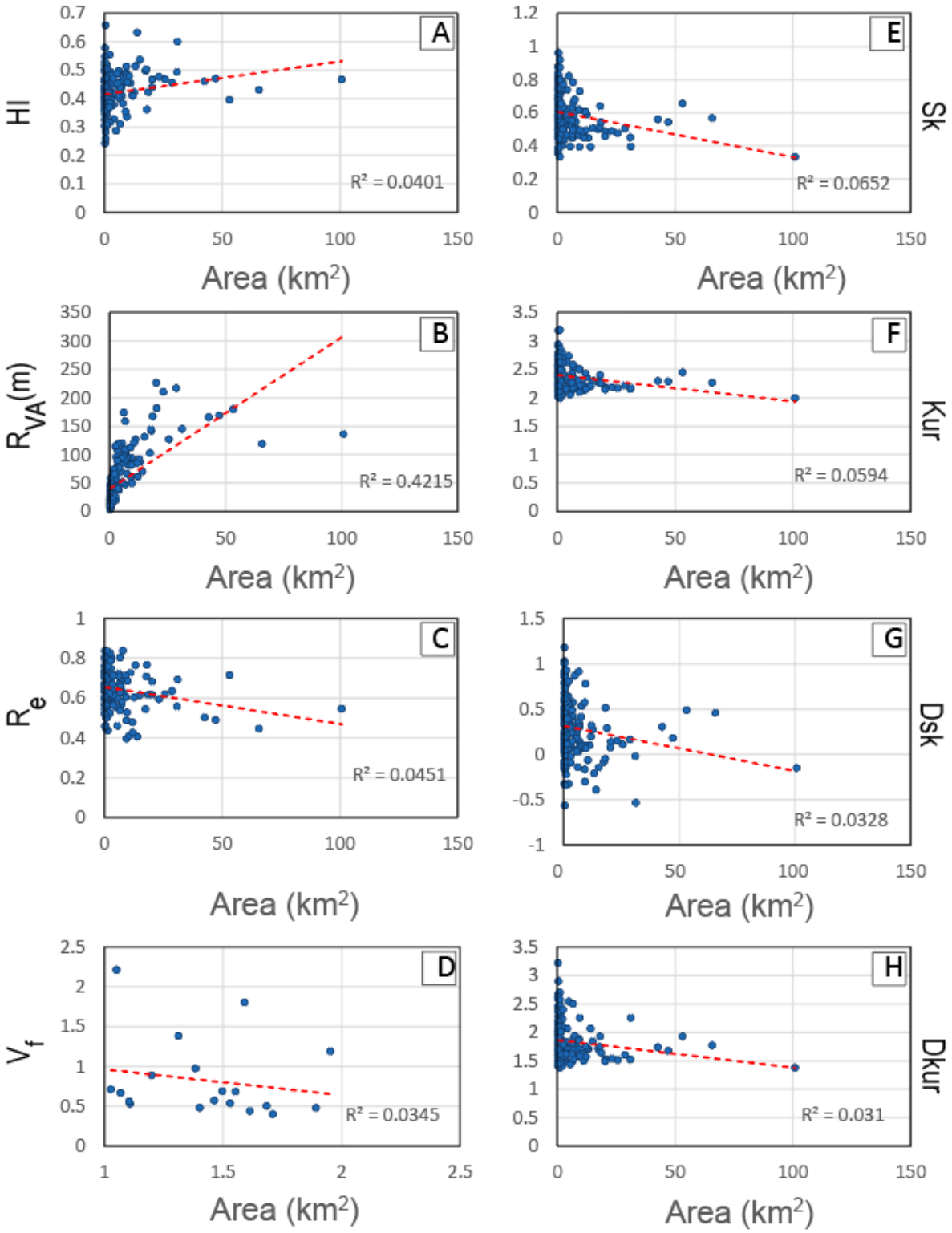

Figure S30. Geomorphic indices vs. area correlation graphs for Valle Fertil Fault. A) Hypsometric Integral (HI). B) Volume-to-Area Ratio (R_{VA}). C) Basin Elongation Ratio (R_e). D) Valley floor width-to-height Ratio (V_f). E) Skewness (Sk). F) Kurtosis (Kur). G) Density Skewness (Dsk). H) Density Kurtosis (Dkur).

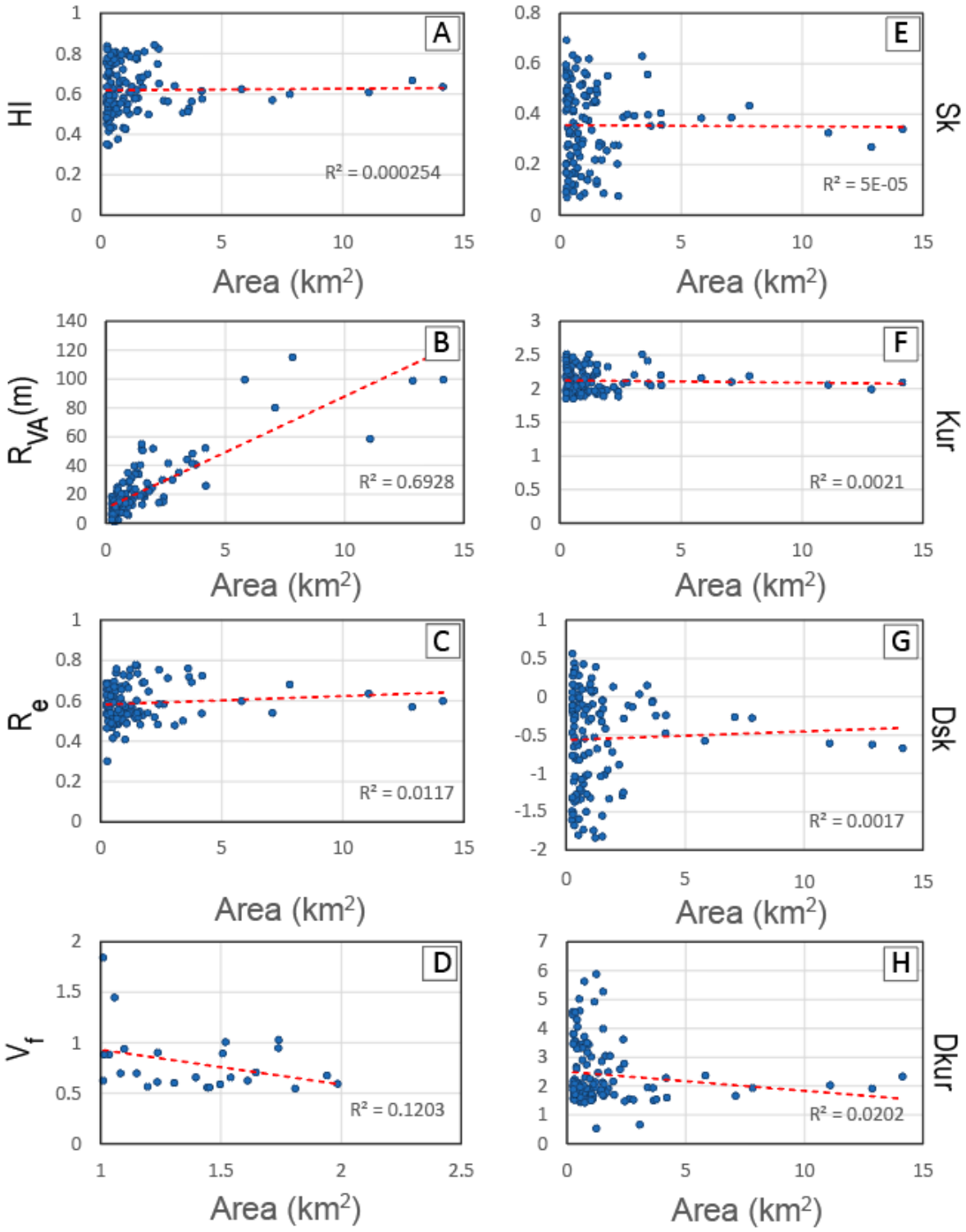

Figure S31. Geomorphic indices vs. area correlation graphs for Sierra de los Llanos and Sierra de las Minas y Ulapes Fault. A) Hypsometric Integral (HI). B) Volume-to-Area Ratio (R_{VA}). C) Basin Elongation Ratio (R_e). D) Valley floor width-to-height Ratio (V_f). E) Skewness (Sk). F) Kurtosis (Kur). G) Density Skewness (Dsk). H) Density Kurtosis (Dkur).

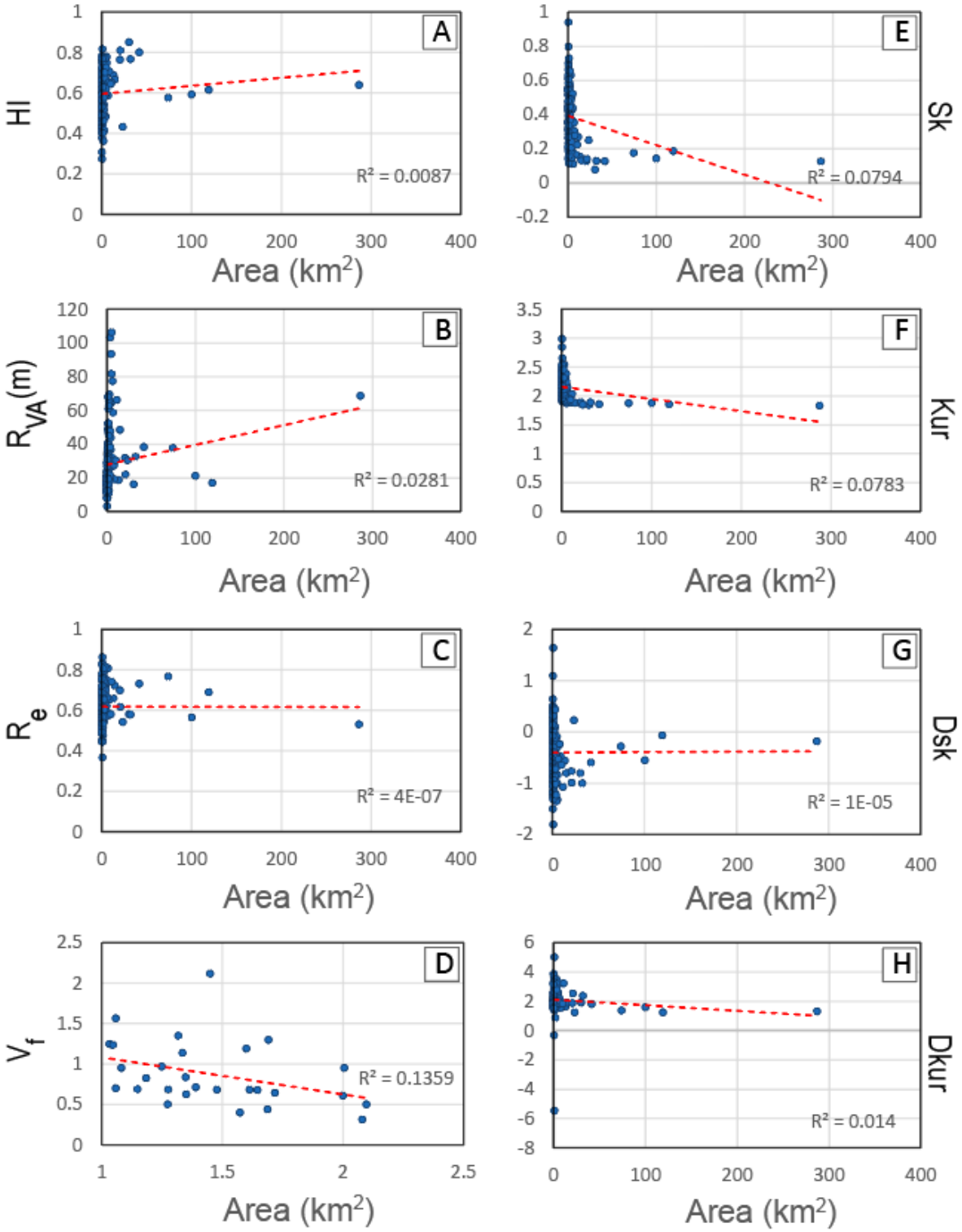

Figure S32. Geomorphic indices vs. area correlation graphs for Pocho Fault. A) Hypsometric Integral (HI). B) Volume-to-Area Ratio (R_{VA}). C) Basin Elongation Ratio (R_e). D) Valley floor width-to-height Ratio (V_f). E) Skewness (Sk). F) Kurtosis (Kur). G) Density Skewness (Dsk). H) Density Kurtosis (Dkur).

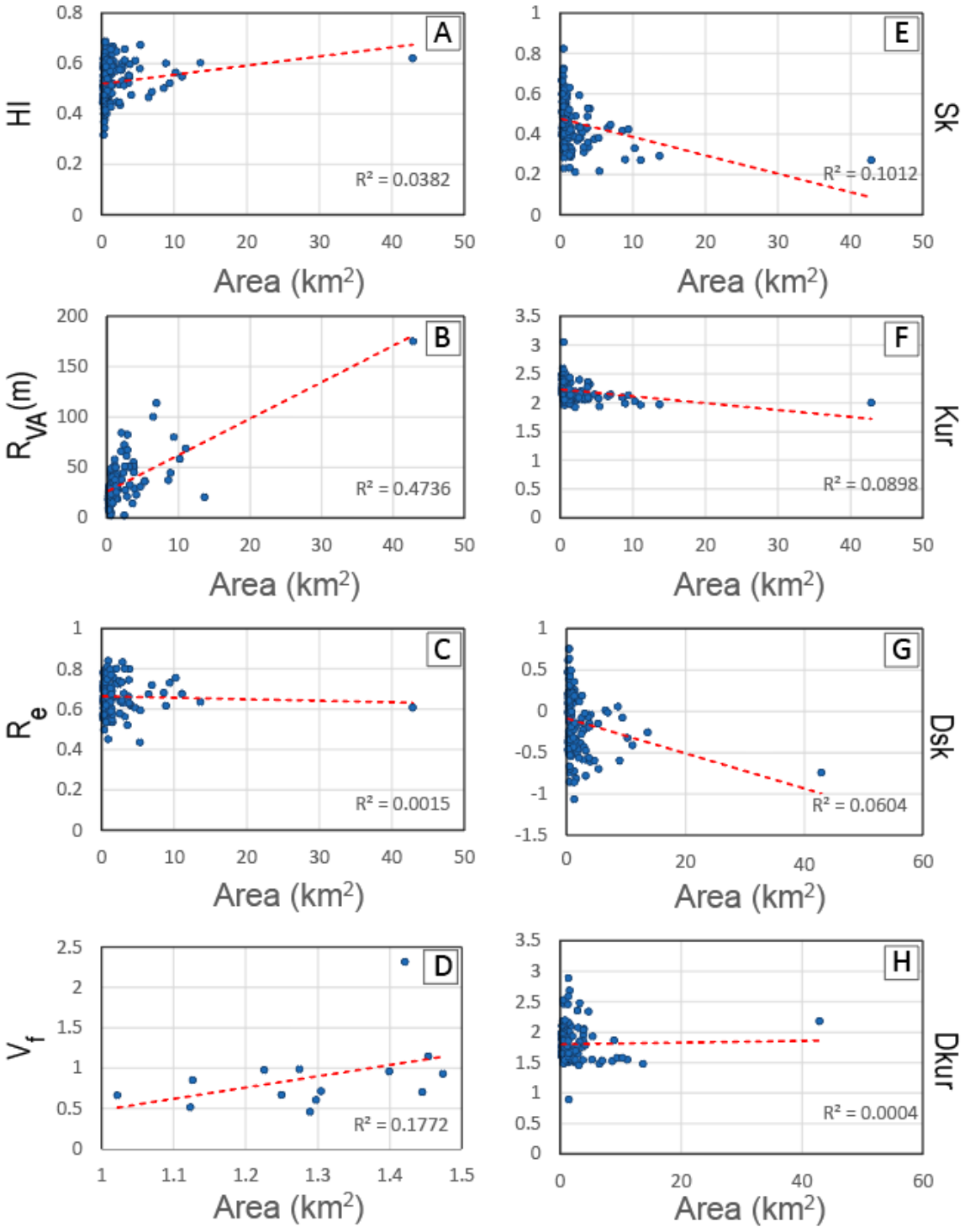

Figure S33. Geomorphic indices vs. area correlation graphs for Sierra Chica Fault Zone. A) Hypsometric Integral (HI). B) Volume-to-Area Ratio (R_{VA}). C) Basin Elongation Ratio (R_e). D) Valley floor width-to-height Ratio (V_f). E) Skewness (Sk). F) Kurtosis (Kur). G) Density Skewness (Dsk). H) Density Kurtosis (Dkur).

	a	b	c	d	e	f	g	h	i	j
HI	0.53 ± 0.06	0.55 ± 0.06	0.52 ± 0.06	0.54 ± 0.08	0.47 ± 0.09	0.49 ± 0.08	0.42 ± 0.06	0.63 ± 0.13	0.58 ± 0.1	0.53 ± 0.08
Re	0.61 ± 0.1	0.62 ± 0.09	0.65 ± 0.1	0.61 ± 0.1	0.51 ± 0.1	0.52 ± 0.13	0.66 ± 0.09	0.58 ± 0.1	0.61 ± 0.1	0.66 ± 0.08
VA	32.81 ± 31.95	54.95 ± 24.89	48.67 ± 36.44	25.55 ± 14.53	35.58 ± 38.31	63.72 ± 65.56	57.27 ± 48.04	24.7 ± 23.99	33.88 ± 20.44	32.76 ± 20.09
VF	0.74 ± 0.31	0.74 ± 0.58	0.71 ± 0.07	0.63 ± 0.28	1.09 ± 0.39	0.61 ± 0.37	0.72 ± 0.36	0.78 ± 0.32	0.69 ± 0.26	0.89 ± 0.5
MFS	1.78 ± 0.19	1.31 ± 0.13	1.74 ± 0.29	1.25 ± 0.14	1.85 ± 0.33	1.52 ± 0.11	1.97 ± 0.32	1.23 ± 0.09	1.71 ± 0.13	1.82 ± 0.24

Table S1. Average of each geomorphic index per fault. Rows correspond to geomorphic indices and columns correspond to faults labelled as follows: a—Eastern Sierra del Tigre Fault. b— Eastern Sierra de Cantera Fault. c—Sierra de Osamentas Fault. d— Morados-Villicum-Zonda-Pedernal Faults. e— Western Pie de Palo Fault. f— Eastern Pie de Palo Fault. g— Valle Fertil Fault. h— Sierra de los Llanos and Sierra de las Minas y Ulapes Fault. i— Pocho Fault. j— Sierra Chica Fault Zone. Red, peach, and grey indicates high, moderate, and low relative uplift rates, respectively.

Text S1. R_{VA} shows a slight correlation with drainage basin area (Fig S23b-S32b), which is expected because in addition to indicating relative uplift rates, R_{VA} can also describe maturity of fault bounded drainage basins, and mature basins tend to be larger. We only included a few large basins in our study, and these showed no or insignificant correlation with other geomorphic indices. Furthermore, when interpreting R_{VA} values for along-strike relative activity of each fault, we were cautious in interpreting these high R_{VA} values as being solely indicative of uplift.

Text S2. Eastern Sierra del Tigre Fault (ETF)

The Eastern Sierra del Tigre fault exhibits a single segment, oriented N12E, with overall increasing relief towards the south (except at fault tips). With the exception of VA, the values of geomorphic indices indicate moderate to high relative uplift rates for most of the length of the fault (**Fig. S4a-h**). The southward increase in maximum and mean k_{sn}, decrease in S_{mf} and V_f ratio, and presence of high VA ratios in the south most likely indicate a slightly higher uplift rate towards the south of the fault. If we take the swath topographic profile as representative of the amount of cumulative displacement on a single fault, then the cumulative displacement which is higher in the south (i.e., a longer northern fault tip zone) is consistent with the southward trend of increasing relative uplift rate (Densmore et al, 2007). The lower relative uplift rate towards the north could possibly be explained by the long response times of catchments in fault tip zones (Ellis and Barnes, 2015). While there are currently no age constraints, due to its gentle fault tip zone and due the absence of a barrier (bounding fault or other linking segment) in the north, the northern tip of the ETF could possibly still be propagating.

Von Gosen (1992), Ragona et al. (1995), and Cardó and Díaz (2005) map a west-dipping reverse fault on the eastern flank of the Sierra del Tigre, but do not provide any information on its activity. In close proximity, albeit on the western flank of the Sierra del Tigre, Bastias (1985) and Siame et al (1997) document Quaternary active scarps of the ~150-km-long El Tigre Fault exhibiting dominantly right-lateral offset (not to be confused with the 'Eastern Sierra del Tigre Fault' on the eastern flank of the range, the subject of our study). Thus, our work provides the first assessment of the relative activity of this range-bounding fault.

Text S3. Eastern Sierra de la Cantera Fault (ECF)

The Eastern Sierra de la Cantera is divided into two major segments (oriented N13E and N23E) separated by a river valley at ~28 km from the north. Except at fault tips and segment boundaries, the entire range exhibits an overall increasing relief from north to south. Overall trends in k_{sn}, R_{VA}, R_e suggest a southward increase in uplift rate, while HI, S_{mf}, and hypsometric curve statistical moments suggest a southward decrease in uplift rate. R_{VA} (<100 m) and V_f (mostly <1) suggest moderate relative uplift rate, while HI (mostly >0.5), S_{mf} (<1.4), and Re (mostly >0.6), indicate a high relative uplift rate (**Fig. S5a-h**). A possible explanation for a relatively low R_{VA} is that the Eastern Sierra de la Cantera range may be bound by a recently reactivated, out-of-sequence, thrust fault, and is characterized by landforms that haven't entirely responded to a possible recent pulse of activity. Out-of-sequence-thrusts are not uncommon and have previously been documented in the Central Precordillera (Jordan et al., 1993), which encompasses the longitudinal range of the Sierra de la Cantera.

Although trends along the entire length of the fault are unclear, locally, all indices but S_{mf} suggest a northward decrease in relative uplift rate for the northern segment. If we take the swath topographic profile as an estimate of the distribution of cumulative displacement on the ECF, we can infer the fault tip behavior of the northern segment of the fault. The trend of decreasing cumulative displacement and a very gentle and broader northern fault tip zone is consistent with a northward decreasing relative uplift rate on the northern segment due to the longer response times of catchments in fault tip zones (Ellis and Barnes, 2015). Due the absence of a barrier (bounding fault or other linking segment) in the north, it is possible that the northern tip of the ECF is still propagating. The southern tip of the northern segment, on the other hand is likely pinned as its fault tip zone is shorter and steep and is bound to the south by the southern segment of the ECF.

Von Gosen (1992), Ragona et al. (1995), and Ramos and Vujovich (2000) map a west-dipping reverse fault on the eastern flank of the Sierra de la Cantera, but do not provide information on timing and recency of movement. In close proximity, albeit on the western flank of the Sierra de la Cantera, Perucca et al. (2015) and Millán and Perucca (2011) document Quaternary-active reverse fault scarps of the Cantera Fault (**Figs. S2a& S5a**; not to be confused with the 'Eastern Sierra de la Cantera Fault' on the eastern flank of the range, the subject of this study). Consequently, this work provides the first assessment of the relative activity of this range-bounding fault.

Text S4. Sierra de Osamentas Fault (OF)

The Sierra de Osamentas appears to exhibit 4 major segments (oriented N23E, N20E, N23E, and N7E) separated by bends/stepovers at 18, 50, and 65 km from the north, but shows an overall fairly uniform relief throughout, except near the river valley at 15 km and in the northern and southern fault tips where it tapers. While R_{VA}, V_f, and Dkur are inconclusive, all the other indices but R_e indicate a trend of decreasing uplift rate

towards the south. Throughout the length of the fault, there is a similar range of R_e values for basins from north to south, but there is a larger clustering of lower R_e values (<0.5-0.6; more elongated to elongated basins) in southern basins. Basins may be more elongated in the south not necessarily due to relatively higher uplift, but possibly due to the greater extent of stream capture of channels from the opposite flank. With exception to R_{VA} (<100 m) and HI (mostly >0.5), absolute values of V_f (mostly <1), S_{mf} (mostly> 1.4), and R_e (mostly ~0.6), however, indicate mostly moderate relative uplift rates (**Fig. S6a-h**). HI (mostly >0.5), on the other hand, indicates high relative uplift rates. If the swath topographic profile is a good approximation of the amount of cumulative displacement on the OF, then the distribution of cumulative displacement that tapers more gradually towards the southern tip is consistent with geomorphic indices (k_{sn}, S_{mf}, and HI) indicating decreasing relative uplift rate towards the south, due to the longer response times of catchments in fault tip zones (Ellis and Barnes, 2015). While the southern portion may still be growing, it is unlikely to propagate southward significantly due to the presence of the NW-SE trending Sierra del Tontal that may act as a barrier. Uniform cumulative displacement everywhere else (except at river valleys) suggest that segments that comprise the OF may already be hard linked.

Von Gosen (1992), Ragona et al. (1995), and Ramos and Vujovich (2000) mapped a west-dipping range-bounding reverse fault, here called the Sierra de Osamentas Fault (OF), on the eastern flank of the Sierra de Osamentas range. Perucca and Onorato (2011) described the OF as having a markedly rectilinear trace and being associated with faceted spurs, most likely indicating Late Quaternary activity. Along the central and southern portions of the Sierra de Osamentas range, Perucca and Onorato (2011) also mapped up to ~6-km-long, 10 m-high fault (labelled OF-2 on **Fig. S6a** and shown in detail in **Fig. S2c**) scarps on the distal eastern piedmont of the southern portion of the Sierra de Osamentas range (not to be confused with the range-bounding 'Sierra de Osamentas Fault') and documented natural trench exposures showing thrusting of Carboniferous bedrock over Pleistocene sediments. Further north, Lara et al. (2018) documented ~5 m-high scarps of the ~27-km-long Maradona Fault System (labelled MF on **Fig. S6a** and shown in detail in **Fig. S2b**), which also cut through Pleistocene-Holocene sediments.

Text S5. Morados-Villicum-Zonda-Pedernal Faults (MVZPF)

The Morados-Villicum-Zonda-Pedernal ranges exhibit at least 4 major segments (oriented N5W, N12E, N5E, and N12E) separated by gaps (river valleys) at 35, 85, and 140 km from the north. Each segment has nearly uniform relief that tapers at the segment tips. Values of HI (frequently >0.6), S_{mf} (mostly< 1.4), Re (mostly 0.5-0.7), and V_f values (<1) indicate nearly uniform relatively high uplift along the Morados, Villicum, Zonda, and Pedernal segments. Low VA values (<100 m) could possibly indicate actively uplifting immature basins, rather than low uplift rates (**Fig. S7a-h**). If the swath topographic profile is taken as a representation of the amount of cumulative displacement on these four faults, then the symmetric cumulative displacement on each fault segment is consistent with generally uniform uplift rate that tapers at the tips (Densmore et al, 2007). The fault tip zones at segment boundaries are long and gently sloping, indicating that the fault segments could still be propagating and may eventually link with each other; incipient linkage seems to be reflected in the topography between the Zonda and Pedernal segments. The northern tip zone of the northernmost Morados segment is similarly long and gently sloping and there is no bounding structure directly north of it, so northward propagation is possible. On the

other hand, the short and steep southern fault tip zone of the southernmost Pedernal segment might suggest that this fault tip is pinned. If so, this could be explained by the presence of a more NW-SE trending Sierra de las Higueras that may be acting as a barrier.

Uniformly moderate-to-high relative uplift rates inferred from geomorphic indices measured along the Morados, Villicum, Zonda, and Pedernal segments is corroborated by documentation of Quaternary activity and/or rupture, and measurement of slip rates of same order of magnitude on Quaternary-active faults found along each of these segments. The La Laja Fault (LF; **Figs. S3a& S7a**) on the eastern flank of the southern Villicum segment has an average shortening rate of ~1 mm/yr (Rockwell, et al., 2014); and the La Rinconada Fault (RF; **Figs. S7a& S2e**) along most of the eastern flank of the Zonda segment, ~0.4 mm/yr (Rimando et al., 2019) and the Las Tapias Fault (TF; **Figs. S7a& S2f**) on the western flank of the Villicum-Zonda transition, ~1 mm/yr (Siame et al., 2002). These similar slip rates, which were measured over the Early Holocene to Late Pleistocene, indicates that these segments may have had uniform, relatively high activity over this duration. The Zonda segment, albeit currently without measured slip rates, also exhibits Quaternary-active scarps (**Figs. S7a& S2d**).

Text S6. Western Pie de Palo Fault (WPF)

The western flank of the Sierra Pie de Palo exhibits 2 segments (oriented N16E and N132E) based on change in orientation at 50 km from the north. There is higher relief in the north (at around 10-40 km), with maximum elevations reaching as high as ~3100 m, which tapers towards the south. Higher maximum k_{sn} and lower Smf in the central and northern portions of the fault, respectively, may indicate higher relative uplift rate in the north to central portions. However, except for R_e and HI (mostly >0.5), actual values of most indices indicate almost uniformly low-to-moderate uplift rates: R_{VA} (mostly <100 m), V_f (mostly > 1), S_{mf} (mostly> 1.4). R_e values (~0.3-0.7), which are indicative of elongated to very elongated basins, could reflect development of streams on NE-SW and NW-SE conjugate fractures which define the topographic fabric of the Sierra Pie de Palo, particularly on its western flank (**Fig. S8a-h**). If the swath topographic profile can be taken as a proxy for the amount of cumulative displacement on a single fault, then the cumulative displacement is skewed to the south (i.e., a longer northern fault tip zone) and is consistent with higher relative uplift rate in the north and central portions (Densmore et al, 2007). It is possible that the lower cumulative displacement in the south may be due to later initiation of movement along the southern segments which hasn't been completely equilibrated yet. If so, then the relative uplift rate towards the south could possibly be explained by the long response times of catchments in fault tip zones (Ellis and Barnes, 2015). While there are currently no age constraints, due to its gentle fault tip zone and due the absence of a barrier (bounding fault or other linking segment) in the south, the southern tip of the WPF could possibly still be propagating. On the other hand, the northern fault tip, which is characterized by a much steeper tip zone is most likely fixed due to the Pajaritos fault which bounds Sierra Pie de Palo to the north.

Ragona et al. (1995) and Ramos and Vujovich (2000) map an east-dipping reverse fault on the western flank of the Sierra Pie de Palo, but do not provide information on timing and recency of movement. Bellahsen et al. (2016) and Siame et al. (2015) describe the fault on the western boundary of the Pie de Palo as inactive based on observation of its very sinuous trace (consistent with our findings), gentler slope of its flank, and of very

poorly incised bordering alluvial fans. While Bellahsen et al. (2016) describe the sinuosity of the Western Pie de Palo, they do not provide any quantitative measure such as S_{mf}.

Text S7. Eastern Pie de Palo Fault (EPF)

The eastern flank of the Sierra Pie de Palo exhibits a single segment, oriented N16E, with similar relief as the western flank of the Sierra Pie de Palo. Except for R_{VA}, HI, Vf, S_{mf}, and R_e indicate relatively higher uplift rates towards the south. While HI itself lacks an along-strike trend, a southward increasing trend in Sk, Kur, and Dsk and Dkur values corroborate the high actual values of V_f, S_{mf}, and R_e in the south. Generally lower VA in the south could possibly reflect youthful, actively uplifting basins. In addition, southward decreasing relief, despite higher uplift rate, may be a result of more recent initiation of movement on the southern extent of the fault. Finally, regardless of along-strike trends, actual values of HI (>0.5) and Re (~0.3-0.7) indicate high relative uplift rates for the entire fault, while R_{VA} (abundant > 100 m), Vf (mostly <1), and S_{mf} (mostly~ 1.4) indicate moderate relative uplift rates for the entire fault (**Fig. S9a-h**). With a very similar swath topographic profile, and consequently similar assumed distribution of cumulative displacement as the western Pie de Palo Fault, the uniform distribution of high relative uplift rate, with some indices (HI, Re, and S_{mf}) indicating even higher rates in the south, may suggest that the landforms (catchments and mountain front) of the southern portion of the Sierra Pie de Palo have started to equilibrate (Ellis and Barnes, 2015). Uniform high relative uplift rate, with possibly even higher relative uplift rates in the south, despite lower relief in the south, further supports the possibility raised in Text S4 that the southern tip of the EPF could possibly be propagating.

In the vicinity of the EPF, recent deformation was documented mostly after the M_S 7.4 1977 Caucete earthquake. While interpretations of the location and vergence of the causal fault associated with the 1977 earthquake from seismicity data were initially conflicting (Langer and Bollinger 1988 and Kadinsky-Cade, et al., 1985), there is consensus now from integration of post-earthquake levelling survey data with higher resolution microseismicity data (Regnier et al., 1992) and interpretation of seismic reflection profiles (Zapata, 1998), that the earthquake occurred on the west-dipping EPF (Bellahsen et al, 2016; Siame et al., 2015). However, only secondary surface rupture on the nearby east-dipping Ampacama-Niquizanga faults (**AF & NF in Fig. S9a**) was documented (Costa et al., 2000), leading most workers to interpret the EPF as a blind fault (Bellahsen et al, 2016; Siame et al., 2015; Kadinsky-Cade et al., 1985). Siame et al. (2015) estimates 0.5±0.1 mm/yr to 0.8±0.4 mm/yr slip rates on the EPF. Nonetheless, whether the EPF is blind or not, geomorphic indices along this mountain front serve to appraise the relative uplift rate of the EPF's underlying structure. Another structure in the vicinity, to the north of the EPF, is the Pajaritos Fault (PF; **Figs. S9a& S3b**)—an ~26-km-long, nearly east-west-oriented oblique-reverse fault with a sinistral sense of displacement. This fault has Holocene and Pleistocene uplift rates of 0.6± 0.4 and 1.0 ± 0.4 mm/yr, respectively, which are compatible with, and comprise a significant proportion of, the geological (Zapata and Allmendinger, 1996; Zapata, 1998; Ramos et al., 2002) and decadal GPS-derived slip rates (Brooks et al., 2003).

Text S8. Valle Fertil Fault (VF)

The Valle Fertil range exhibits 4 segments (N28W, N15W, N20W, and N25W) separated from each other by bends/stepovers at 45, 110, and 165 km from the north, all with nearly uniform relief that tapers at the tips of each segment. The trend of nearly uniform values for most indices (except for low S_{mf} at tips) suggests a uniform uplift rate for most of the length of the fault. Lower S_{mf} at the northern and southern fault tips suggest elevated uplift rates which may possibly be due to incipient lateral fault propagation to the north and south. V_f (mostly < 1), HI (mostly 0.4-0.5), VA (<<100 m average), S_{mf} (mostly> 1.4), and Re (~0.55-0.8) indicate uniform, moderate relative uplift rates along this fault (**Fig. S10a-h**). If the swath topographic profile is a good approximation of the amount of cumulative displacement on the Valle Fertil Fault, then the distribution of cumulative displacement that reflects 4 segments, together with nearly uniform relative uplift rate throughout the fault inferred from the geomorphic indices suggest that these segments may already be hard linked (Densmore et al, 2007). The northern and southern fault tip zones are characterized by lower k_{sn} suggesting lower uplift rates, which is to be expected but not necessarily conclusive, due to the longer response times of catchments in fault tip zones (Ellis and Barnes, 2015). In contrast, S_{mf} which indicates higher relative uplift rates at the tips, may be more reliable as it is insensitive to the amount of cumulative displacement of the range. The northern tip is shorter and steeper and already has relatively high relief ranges to its north. Consequently, although northward propagation is possible, fault growth in the north is likely dominated by linkage, if any. On the other hand, the high relative uplift rate, and longer and gentler southern fault tip zone and the presence of only very low relief linear bedrock exposures to the south suggest that southward propagation is still possible.

Furque et al. (1998), Ragona et al. (1995), Ramos and Vujovich (2000), and Vujovich et al. (1998) map an east-dipping reverse fault on the western flank of the Sierra de Valle Fertil and Rothis et al. (2018) document Quaternary scarps of the similarly east-dipping Las Chacras Fault (CF; **Figs. S3c& S10a**) on the piedmont of the southern tip of this range. Ortiz et al. (2015) documented a trend of younging deformation in the northern and southern tips of the Sierra de Valle Fertil Fault since the Pliocene from thermochronological dating. They further noted similarity of this pattern to locations of most likely more recent, Quaternary deformation features and shallow crustal seismicity (e.g., Kadinsky-Cade et al., 1985) also to the north and southern tips, suggesting a consistency of younging deformation towards the tips on different time scales. This high activity towards the tips further supports the theory of longer response times in fault tip zones as an explanation for low relative uplift rate from geomorphic indices.

Text S9. Sierra de los Llanos & Sierra de las Minas y Ulapes Faults (LMUF)

The Sierra de los Llanos Fault (LF) to the north and the Sierra de las Minas y Ulapes Fault (MUF) to the south are individual faults (oriented N30W and N-S, respectively) which are separated by a ~60 km. LF and MUF are characterized by relief that higher in the south and to the north, respectively. Actual values suggest conflicting levels of relative uplift rates. HI (mostly >0.6), S_{mf} (mostly< 1.4), and R_e (mostly 0.5-0.7), indicate mostly high relative uplift rates for both faults (with HI and S_{mf} indicating higher uplift rates on the Sierras de las Minas y Ulapes Fault in the south), while V_f (mostly > 0.5) indicates moderate relative uplift rates. On the other hand, R_{VA} (<100 m) indicates low relative uplift rates for both faults. Overall, the geomorphic indices may still reflect relatively high uplift rate if we interpret the VA values as indicative of predominantly lateral erosion that haven't picked up yet with more recent higher uplift rates (**Fig. S11a-h**). If the

swath topographic profile appropriately represents the distribution of cumulative displacement on these two faults, then cumulative displacement on the Llanos Fault and Minas Y Ulapes Fault is skewed to the south and to the north, respectively. The trend of relative uplift rate suggested by k_{sn} and VA ratio seem to mimic this distribution. The long, gentle northern tip zone and narrow, steep southern tip zone of the Llanos Fault could possibly be explained by a fault that is fixed in the south and is propagating northward. Similarly, the long, gentle southern tip zone and narrow, steep northern tip zone of the Minas Y Ulapes Fault could possibly be explained by a fault that is fixed in the north and is propagating southward (Ellis and Barnes, 2015).

Caselli et al. (1999) and Guerrero et al. (1993), map west-dipping reverse faults on the eastern flanks of the Sierra de los Llanos and the Sierra de las Minas y Ulapes ranges, but do not provide information on timing and recency of movement. Therefore, this study provides the first assessment of the relative activity and presence of Quaternary-active scarps (e.g., Llanos Fault, labelled as LF on **Fig. S11a** and shown in detail in **Fig. S3d**) along this range-bounding fault.

Text S10. Pocho Fault

The Sierra de Pocho range exhibits 3 segments (oriented N10E, N15W, and N15W) separated from each other by bends or stepovers at 15 and 115 km from the north. The entire fault exhibits an overall uniform relief that tapers at its northernmost and southernmost fault tips (**Fig. S12**)**.** Vf (mostly <1) and S_{mf} (mostly> 1.4) indicate uniform, moderate relative uplift rates, while R_{VA} (<100 m) indicates low relative uplift rates. HI values (north: 0.6-0.8; south: 0.4-0.7), which in most cases are only in the range of 0.5 to 0.6, are higher in the north, a finding that is corroborated by a southward decreasing trend in Sk, Kur, and Dsk, indicates higher uplift rates in the north than in the south. R_e (mostly ~0.5-0.8; some <0.5 in the center), suggests generally high relative uplift rates, with some basins in the center indicating higher uplift rates. In summary, the values along the Pocho Fault suggest relatively higher uplift rates in northern and central portions (**Fig. S12a-h**). If we take the swath topographic profile as representative of the amount of cumulative displacement on a single fault, then the slightly lower cumulative displacement and longer fault tip zone in the southern tip is consistent with the lower relative uplift rates inferred from geomorphic indices for the southern portion (Densmore et al, 2007). It is possible that the lower cumulative displacement in the south may represent a displacement 'deficit', which may be due to linkage of a southern fault of lower cumulative displacement with a much larger northern fault of higher cumulative displacement which hasn't been completely equilibrated yet. It is also possible that the southern portion represents a linkage zone between the Pocho Fault and the Comechingones Fault to its south. Either way, the lower relative uplift rate towards the south of the Pocho Fault could possibly be explained by the long response times of catchments in fault tip zones of growing faults (Ellis and Barnes, 2015).

Bonalumi et al. (1999) and Candiani et al. (2001) map an east-dipping reverse fault on the western flank of the Sierra de Pocho, but do not provide information on its activity.

Costa et al. (2014) is the first to demonstrate the recent activity of the Pocho Fault (PF; **Fig. S12a** and **Fig. S3e**) of this range-bounding fault.

Text S11. Sierra Chica Fault Zone (SCFZ)

The Sierra Chica range exhibits 3 segments (oriented N15W, N10W, and N18W) separated from each other at 75 and 130 km from the north, all with nearly uniform relief that tapers at the tips of each segment. With exception to VA (mostly <100 m), V_f (mostly <1) and S_{mf} (mostly> 1.4), Re (~0.6-0.8), and HI (mostly >0.5) indicate mostly moderate relative uplift rates for the entire length of the fault, average values of , low to moderate (**Fig. 13a-h**). If we take the swath topographic profile as an approximation of the distribution of cumulative displacement on the SCFZ, then the cumulative displacement distribution which tapers at the tips is at least consistent with generally higher relative uplift rates towards the center and lower relative uplift rates towards the tips suggested by k_{sn} and S_{mf}. The lack of a consistent trend in relative uplift rate from other indices in relation to segment linkage in the central portion of the fault, could either be a spatial resolution issue of geomorphic indices on this particular fault (basins on which geomorphic indices are measured are too few to sufficiently characterize the short fault segments and linkage zones) or could also possibly indicate the SCFZ's segments may almost entirely be hard linked.

The northern portion of the SCFZ, the Cosquin segment (C; **Figs. S3f & 13a**) was the epicentral area of the 1947 M 6.5 Giardino earthquake. However, no surface rupture was documented. Based on outcrop exposures, the Carlos Paz (CP, central); and Santa Rosa (SR) and Potrero de Garay (PG, southern) segments, ~70 and 120 km from northern tip, respectively, have been active in the Quaternary. However, Holocene activity is uncertain due to the lack of convincing geomorphic and stratigraphic indications (Costa et al., 2000; Costa et al., 2001a; Costa et al. 2014; and Richardson et al., 2013, and references therein).

References

Bastías, H. (1985). Fallamiento Cuaternario en la región sismotectónica de Precordillera (Doctoral dissertation, Tesis Doctoral). Facultad de Ciencias Exactas, Físicas y Naturales, Universidad Nacional de San Juan.

Bellahsen, N., Sébrier, M., & Siame, L. (2016). Crustal shortening at the Sierra Pie de Palo (Sierras Pampeanas, Argentina): near-surface basement folding and thrusting. Geological Magazine, 153(5-6), 992-1012.

Bonalumi, A., Martino, R., Baldo, E., Zarco, J. Sfragulla, J., Carignano, C., Kraemer, P., Escayola, M., Tauber, A., Cabanillas, A., Juri, E., & Torres, B. (1999). Memoria Hoja geológica 3166-IV, Villa Dolores. Servicio Geológico Minero Argentino, Buenos Aires.

Brooks, B., Bevis, M., Smalley, R., Kendrick, E., Manceda, R., Lauría, E., et al. (2003). Crustal motion in the southern Andes (26°–36°S): Do the Andes behave like a microplate? Geochemistry, Geophysics, Geosystems, 4(10), 1085. https://doi.org/10.1029/2003GC000505

Candiani, J., Carignano, C., Stuart-Smith, P., Lyons, P., Miró, R., & López, H. (2001). Memoria Hoja geológica 3166-II, Cruz del Eje. Servicio Geológico Minero Argentino, Buenos Aires.

Cardó, R., Díaz, I. N. (2005). Memoria Hoja Geológica 3169-I, Rodeo. Servicio Geológico Minero Argentino, Buenos Aires.

Caselli, A., Net, L., Litvak, V., Limarino, C., Poma, S., & Gutierrez, P. (1999). Memoria Hoja Geológica 3166-I, Chamical. Servicio Geológico Minero Argentino, Buenos Aires.

Costa, C., Machette, M. N., Dart, R., Bastías, H., Paredes, J., Perucca, L. P., Tello, G., & Haller, K. (2000). Map and database of Quaternary faults and folds in Argentina. US Geological Survey Open-File Report, 108, 75.

Costa, C. H., Gardini, C. E., Chiesa, J. O., Ortíz Suárez, A. E., Ojeda, G. E., Rivarola, D. L., ... & Guerstein, P. G. (2001). Hoja Geológica 3366-III San Luis. Servicio Geológico Minero Argentino, Buenos Aires.

Costa, C., Massabie, A., Sagripanti, G., Brunetto, E., & Coppolecchia, M. (2014). Neotectónica de la provincia de Córdoba. In Geología y Recursos Naturales de la Provincia de Córdoba, Relatorio del XIX Congreso Geológico Argentino (pp. 725-748).

Densmore, A. L., Gupta, S., Allen, P. A., & Dawers, N. H. (2007). Transient landscapes at fault tips. Journal of Geophysical Research: Earth Surface, 112(F3).

Ellis, M. A., & Barnes, J. B. (2015). A global perspective on the topographic response to fault growth. Geosphere, 11(4), 1008-1023.

Furque, G., González, P., & Caballé, M. (1998). Descripción de la hoja geológica 3169-II, San José de Jáchal (Provincias de San Juan y La Rioja). Servício Geológico y Minero Argentino Boletín 259.

Guerrero, M., Lavandaio, E., & Marcos, O.(1993) Mapa geológico de la provincia de La Rioja escala 1: 500,000. Dirección Nacional del Servicio Geológico, Secretaría de Minería República Argentina.

Jordan, T. E., Allmendinger, R. W., Damanti, J. F., & Drake, R. E. (1993). Chronology of motion in a complete thrust belt: The Precordillera, 30–31°S, Andes Mountains. The Journal of Geology, 101(2), 135–156. https://doi.org/10.1086/648213

Kadinsky-Cade, K., Reilinger, R., & Isacks, B. (1985). Surface deformation associated with the November 23, 1977, Caucete, Argentina, earthquake sequence. Journal of Geophysical Research, 90(B14), 12,691–12,700. https://doi.org/10.1029/JB090iB14p12691

Langer, C. J., & Bollinger, G. A. (1988). Aftershocks of the western Argentina (Caucete) earthquake of 23 November 1977: some tectonic implications. Tectonophysics, 148(1-2), 131-146.

Lara, G., Perucca, L., Rothis, M., Pantano, A., & Sáez, M. (2018). Actividad tectónica cuaternaria del Sistema de Falla Maradona, Precordillera Central, Argentina. Andean geology, 45(2), 145-160.

Millán, J. L., & Perucca, L. P. (2011). Análisis neotectónico del extremo norte del sobrecorrimiento La Cantera, provincia de San Juan, Argentina. Revista Mexicana de Ciencias Geológicas, 28(3), 337-348.

Ortiz, G., Alvarado, P., Fosdick, J. C., Perucca, L., Saez, M., & Venerdini, A. (2015). Active deformation in the northern Sierra de Valle Fértil, Sierras Pampeanas, Argentina. Journal of South American Earth Sciences, 64, 339-350.

Perucca, L. P., & Onorato, R. (2011). Fallas con actividad cuaternaria en el corredor tectónico Matagusanos-Maradona-Acequión entre los ríos de La Flecha y del Agua, provincia de San Juan. Revista de la Asociación Geológica Argentina, 68(1), 39-52.

Perucca, L., Rothis, M., Bezerra, F. H., Vargas, N., & Lima, J. (2015). Late quaternary evolution of the La Cantera Fault System (Central Precordillera, Argentina): A morphotectonic and paleoseismic analysis. Tectonophysics, 661, 200-209.

Ragona, D., Anselmi, G., Gonzalez, P., & Vujovich, G. (1995). Mapa geológico de la provincial de San Juan escala 1: 500,000. Dirección Nacional del Servicio Geológico, Secretaría de Minería República Argentina.

Ramos, V. A., & Vujovich, G. I. (2000). Hoja Geológica 3169-IV, San Juan, Provincia de San Juan. Subsec. Minería Nación, Servicio Geológico Minero Argentino, Buenos Aires, Boletín 243 (p. 82).

Ramos, V. A., Cristallini, E. O., & Pérez, D. J. (2002). The Pampean flat-slab of the Central Andes. Journal of South American earth sciences, 15(1), 59-78.

Regnier, M., Chatelain, J. L., Smalley Jr, R., Chiu, J. M., Isacks, B. L., & Araujo, M. (1992). Seismotectonics of Sierra Pie de Palo, a basement block uplift in the Andean foreland of Argentina. Bulletin of the Seismological Society of America, 82(6), 2549-2571.

Richardson, T., Ridgway, K. D., Gilbert, H., Martino, R., Enkelmann, E., Anderson, M., & Alvarado, P. (2013). Neogene and Quaternary tectonics of the Eastern Sierras Pampeanas, Argentina: Active intraplate deformation inboard of flat-slab subduction. Tectonics, 32(3), 780- 796.

Rimando, J. M., Schoenbohm, L. M., Costa, C. H., Owen, L. A., Cesta, J. M., Richard, A. D., & Gardini, C. E. (2019). Late Quaternary Activity of the La Rinconada Fault Zone, San Juan, Argentina. Tectonics, 38(3), 916-940.

Rockwell, T.K., Keller, E.A. and Johnson, D.L. (1985). Tectonic Geomorphology of Alluvial Fans and Mountain Fronts near Ventura, California. In: Morisawa, M., Ed., Tectonic Geomorphology. Proceedings of the 15th Annual Geomorphology Symposium, Allen and Unwin Publishers, Boston, 183-207.

Rothis, L. M., Perucca, L. P., Malnis, P. S., Zuñiga, A. P., Alcacer, J. M., Haro, F. M., & Vargas, N. (2018). Análisis morfotectónico en el piedemonte suroccidental del antepais andino, Sierras Pampeanas Occidentales, San Juan, Argentina. Geosciences= Geociências, 37(1), 55-74.

Siame, L. L., Bourlès, D. L., Sébrier, M., Bellier, O., Castano, J. C., Araujo, M., et al. (1997). Cosmogenic dating ranging from 20 to 700 ka of a series of alluvial fan surfaces affected by the El Tigre fault, Argentina. Geology, 25(11), 975-978.

Siame, L. L., Bellier, O., Sébrier, M., Bourlès, D. L., Leturmy, P., Perez, M., & Araujo, M.(2002). Seismic hazard reappraisal from combined structural geology, geomorphology and cosmic ray exposure dating analyses: The eastern Precordillera thrust system (NW Argentina). Geophysical Journal International, 150(1), 241–260. https://doi.org/10.1046/j.1365-246X.2002.01701.x

Siame, L. L., Sébrier, M., Bellier, O., Bourlès, D., Costa, C., Ahumada, E. A., et al. (2015). Active basement uplift of Sierra Pie de Palo (northwestern Argentina): Rates and inception from 10Be cosmogenic nuclide concentrations. Tectonics, 34, 1129–1153. https://doi.org/10.1002/2014TC003771

Von Gosen, W. (1992). Structural evolution of the Argentine Precordillera: The Río San Juan section. Journal of Structural Geology, 14(6), 643-667.

Vujovich, G., Chernicoff, J., Tchiliguirian, P., Godeas, M., Marín, G., Pezzutti, N., & Sepúlveda, E. (1998). Hoja geológica 3166-III, Chepes, provincias de San Juan y La Rioja. Servicio Geológico Minero Argentino.

Zapata, T. R. (1998). Crustal structure of the Andean thrust front at 30 S latitude from shallow and deep seismic reflection profiles, Argentina. Journal of South American Earth Sciences, 11(2), 131-151.

Zapata, T. R., & Allmendinger, R. W. (1996). Thrust-front zone of the Precordillera, Argentina: a thick-skinned triangle zone. AAPG bulletin, 80(3), 359-381.